



Probing the structure and mechanical properties of the graphite nodules in ductile cast irons via nano-indentation

Andriollo, Tito; Fæster, Søren; Winther, Grethe

Published in:
Mechanics of Materials

Link to article, DOI:
[10.1016/j.mechmat.2018.03.010](https://doi.org/10.1016/j.mechmat.2018.03.010)

Publication date:
2018

Document Version
Peer reviewed version

[Link back to DTU Orbit](#)

Citation (APA):
Andriollo, T., Fæster, S., & Winther, G. (2018). Probing the structure and mechanical properties of the graphite nodules in ductile cast irons via nano-indentation. *Mechanics of Materials*, 122, 85-95.
<https://doi.org/10.1016/j.mechmat.2018.03.010>

General rights

Copyright and moral rights for the publications made accessible in the public portal are retained by the authors and/or other copyright owners and it is a condition of accessing publications that users recognise and abide by the legal requirements associated with these rights.

- Users may download and print one copy of any publication from the public portal for the purpose of private study or research.
- You may not further distribute the material or use it for any profit-making activity or commercial gain
- You may freely distribute the URL identifying the publication in the public portal

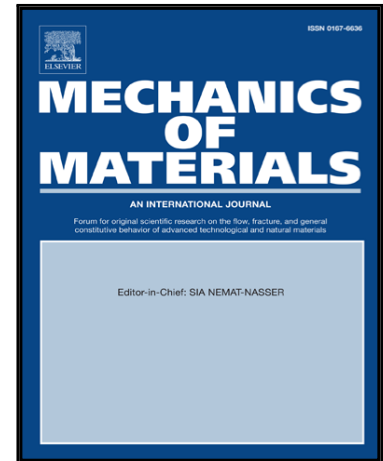
If you believe that this document breaches copyright please contact us providing details, and we will remove access to the work immediately and investigate your claim.

Accepted Manuscript

Probing the structure and mechanical properties of the graphite nodules in ductile cast irons via nano-indentation

Tito Andriollo , Søren Fæster , Grethe Winther

PII: S0167-6636(17)30819-0
DOI: [10.1016/j.mechmat.2018.03.010](https://doi.org/10.1016/j.mechmat.2018.03.010)
Reference: MECMAT 2858



To appear in: *Mechanics of Materials*

Received date: 27 November 2017
Revised date: 7 March 2018
Accepted date: 27 March 2018

Please cite this article as: Tito Andriollo , Søren Fæster , Grethe Winther , Probing the structure and mechanical properties of the graphite nodules in ductile cast irons via nano-indentation, *Mechanics of Materials* (2018), doi: [10.1016/j.mechmat.2018.03.010](https://doi.org/10.1016/j.mechmat.2018.03.010)

This is a PDF file of an unedited manuscript that has been accepted for publication. As a service to our customers we are providing this early version of the manuscript. The manuscript will undergo copyediting, typesetting, and review of the resulting proof before it is published in its final form. Please note that during the production process errors may be discovered which could affect the content, and all legal disclaimers that apply to the journal pertain.

Highlights:

- Nano-indentation tests were made on the cross-section of a graphite particle
- The experimental error alone cannot explain the spatial dependence of the results
- A model based on the particle geometry and internal structure is developed
- The precise particle sub-surface geometry is obtained via 3D tomography
- A clear link between particle structure and mechanical properties is demonstrated

ACCEPTED MANUSCRIPT

Probing the structure and mechanical properties of the graphite nodules in ductile cast irons via nano-indentation

Tito Andriollo^{a,c}, Søren Fæster^b and Grethe Winther^a

^a Department of Mechanical Engineering, Technical University of Denmark, DK-2800 Kgs. Lyngby, Denmark

^b Department of Wind Energy, Technical University of Denmark, Risø Campus Frederiksborgvej 399, DK-4000 Roskilde, Denmark

^c Corresponding author. Full address: Technical University of Denmark, Produktionstorvet, Building 425, room 225, 2800 Kgs. Lyngby, Denmark. Phone: +45 45 25 47 94. E-mail: titoan@mek.dtu.dk

Abstract

Little is known today about the mechanical properties of the graphite nodules, despite the key influence these particles have on the performance of ductile cast irons. To address this issue, nano-indentation tests were performed on the cross-section of a nodule whose sub-surface morphology was characterized via 3D computed tomography. From the recorded load vs. penetration curves, the spatial variation of the maximum indenter penetration h_{\max} and of the reduced Young's modulus E^* was determined. It was observed that the pattern of h_{\max} presents features which, statistically, cannot be explained with the experimental error. Conversely, they can be justified by a model which takes into account the geometrical interaction between the indenter and the local orientation of the graphite platelets forming the nodule. To the authors' best knowledge, this result constitutes the first direct proof of a clear link between internal structure and mechanical properties of the nodules. The existence of a non-negligible mechanical anisotropy implies that the calculated mean value of E^* can only be seen as indicative of a sort of "averaged" elastic stiffness. Caution should then be used when assessing the elastic response of the entire nodule just on the basis of this parameter, as complex anisotropic effects associated with the non-random orientation of the graphite platelets can be foreseen.

Keywords

Nano-indentation; Cast iron; Graphite; Nodule; Structure; Mechanical properties;

Paper structure

Abstract.....	2
Keywords.....	3
1. Introduction	4
2. Material and methods	7
3. Results	10
3.1 Shape of the load vs. penetration curves	10
3.2 Young's modulus calculated using the Oliver & Pharr method.....	12
4. Discussion.....	15
4.1 Interpretation of the results on the basis of the nodule structure.....	15
4.2 Applicability of the Oliver & Pharr method.....	20
5. Conclusions	22
Acknowledgements	23
Authors' contribution	23
References	24

1. Introduction

Modern ductile cast irons (DCIs) are a family of advanced structural materials heavily used in key industrial sectors like automotive, marine and energy production. The importance of DCIs is well captured by the fact that, alone, they account for as much as 25% of the castings produced worldwide [1]. As discussed in [2–4], the reason for their success is at least threefold. First, DCIs are infinitely recyclable and thereby easy to reuse or dispose. Second, these materials are very easy to cast, allowing an efficient production of complex shaped parts. Third, when the specific properties are considered, i.e. the property-to-weight ratios, DCIs offer a combination of strength, toughness and cost which is unrivalled in relation to several applications in the aforementioned sectors.

The unique properties of DCIs are a consequence of the complex material microstructure, which is formed by graphite particles – normally called nodules, or spheroids – of different size and spheroidicity embedded in a steel matrix where multiple phases may coexist depending on chemistry and process conditions. By contrast, a major drawback of this pronounced heterogeneity at the micro-scale is that standard theoretical models, which consider DCIs as homogeneous, are often not effective in describing the material mechanical behavior in conditions other than simple tensile loading [5][6]. Prompted by the recent progress in experimental characterization techniques, which allow unprecedented insight into the morphology and distribution of the microstructural phases, more advanced micro-mechanical and multiscale models are now emerging [7][8][9][10][11][12].

However, as emphasized in a recent review article [13], a major challenge associated with developing this new type of models is the lack of knowledge concerning the mechanical behavior of the individual constituents forming the microstructure of DCIs. This issue is particularly critical for the graphite nodules rather than for the matrix, as revealed by the very large spread existing in the literature concerning data for their elastic properties [14][15]. In this respect, it is worth remarking that the presence of the graphite nodules in DCIs is, in general, not negligible at all. Indeed, the nodules can promote the formation of a significant residual stress field at the micro-scale during manufacturing, due to the thermal contraction mismatch with the surrounding matrix [16], and, more importantly, they can

also strongly affect the crack propagation path during cyclic loading [17][18][19][20]. Both facts indicate that poor knowledge of the mechanical properties of the nodules poses severe limitations to the successful application of advanced multiscale models to DCIs, and, by extension, to the further optimization of the in-service performance of this important class of structural materials.

The difficulties in obtaining reliable data for the properties of the nodules are rooted in their small size, typically in the order of 100 μm , which reduces significantly the number of techniques available for direct mechanical characterization. To the authors' best knowledge, all the experimental studies performed so far have relied on nano-indentation measurements, conducted following the well-known method of analysis proposed by Oliver and Pharr [21]. As reported in Table 1, such studies have ultimately suggested values of the nodules' Young's modulus in the order of 15-30 GPa [10][22][23]. Nevertheless, some researchers [24] have pointed out that, as graphene layers can be easily separated along the basal planes by the action of a sharp nano-indenter, the calculated values of Young's modulus might underestimate considerably the elastic stiffness of the nodule as a whole.

Table 1: Nano-indentation based studies of the mechanical properties of the graphite nodules.

Authors	Type of analysis	Measured Young's modulus	Measured hardness
Dierickx et al, 1996	Oliver & Pharr	15 \pm 5 GPa	0.5 \pm 0.5 GPa
Pradhan et al, 2009	Oliver & Pharr	28 \pm 9 GPa	0.5 \pm 0.3 GPa
Fernandino et al, 2017	Oliver & Pharr	15 \pm 4 GPa	-

More in general, the results of Table 1 are difficult to rationalize on the basis of the thorough Transmission Electron Microscopy (TEM) investigations of the internal structure of the nodules carried out in the last couple of decades [25–30]. Indeed, these have clarified that each nodule consist of a small nucleus containing complex oxides and sulfides, which served as nucleation sites during solidification, and a much thicker outer shell of graphitic nature, which represents the major part of the nodule by volume. As described in [27] and schematically shown in Figure 1, the latter one consists of two parts: a bulk region, formed by oriented graphite platelets arranged into conical sectors radiating from the nodule center

to the outer periphery, and a thin superficial graphite layer, characterized by smaller and highly misoriented crystals. The graphite platelets, which represent the basic building blocks of the nodule, have thicknesses in the sub-micrometer range and consist of graphene layers where the c-axis of the hexagonal unit cell is parallel to the platelet normal [25][28]. The fact that the graphite has a non-uniform yet well-defined crystallographic orientation in the major part of the nodule raises two issues. First, the outcome of a nano-indentation test should be dependent on the location chosen for making the indent. Second, as the graphite platelets are not randomly oriented, their anisotropy should render the response offered to the indenter's penetration anisotropic as well. This last aspect might possibly create some inconsistencies in the application of the Oliver & Pharr method, as the technique is based on an exact analytical solution valid for indentation into an isotropic medium [31].

Figure 1: Schematic of the internal structure of a graphite nodule.

The two issues just discussed have much to do with the extent to which the internal structure of the nodule, as determined from TEM, can impact the mechanical properties of the particle at the micron level. So far, indirect evidence of this link has been documented, mainly via ascertaining that micromechanical models where the internal structure of the nodule is replicated are consistent with both the macroscopic elastic properties of DCIs [32] and the shape of the local residual stress field measured in ferrite grains surrounding the particle [11]. However, no direct proofs of the connection between structure and mechanical properties of the nodules seem to be available in the literature, suggesting that further investigations in this area are needed.

In light of the present discussion, this paper aims at performing new nano-indentation-based analyses of the graphite nodules in DCIs with a twofold purpose. From a scientific viewpoint, the goal is to determine whether or not the internal structure of the nodule affects the nano-indentation results and thereby the local mechanical properties. From an

engineering perspective instead, the aim is to analyze whether the Oliver & Pharr method is applicable to the nodules and whether the calculated values of Young's modulus are meaningful and can be used as input in multiscale models of DCIs.

2. Material and methods

The DCI sample used in the present work was extracted from a large wind turbine main shaft cast in a metal mold. The microstructure consisted of almost spherical graphite nodules embedded in a matrix with a relatively homogeneous structure, being mainly ferrite with a small fraction of pearlite ($\approx 5\%$). The 3D morphology of the graphite nodules within a $1 \times 1 \times \frac{1}{4}$ mm volume near the surface of the sample was characterized by X-ray tomography using a Zeiss Xradia 520 Versa micro computed tomography (μ CT) system. The μ CT scan was acquired with polychromatic and conical X-ray beam with energies up to 150 keV, resulting in a reconstructed 3D density map with a voxel size of 3 μ m. Figure 2 shows the outcome of the μ CT scan. The nodule marked with red arrows, which had the shape of an almost perfect sphere sectioned in its top half by the plane of the sample surface, was selected for further nano-indentation analysis.

Nano-indentation tests were performed on the exposed section of the selected nodule by means of a diamond Berkovich nano-indenter mounted on the NHT² platform from CSM Instruments. Two separate series of indents were made along two mutually perpendicular axes, denoted by s and t as indicated in Figure 3, up to a distance of ≈ 15 μ m from the nodule-matrix boundary. A fixed distance of 10 μ m between consecutive indents was maintained and the origin of each axis was selected as the midpoint between the location of the first and last indent. According to this choice, the intersection point between the axes turned out to have coordinates $s = -15$ μ m and $t = -25$ μ m. Each nano-indent was made by pressing the indenter into the material at a loading rate of 2 mN/min up to a maximum load of 1 mN, followed by 10 s holding time and subsequent unloading at the same speed. During the entire process, the applied load F and the indenter penetration h were recorded at a frequency of 10 Hz.

Each individual F vs. h curve was used to assess the elastic stiffness of the nodule by means of the standard Oliver & Pharr procedure [33]. Accordingly, the unloading part of the F vs. h curve was fitted using the expression

$$F = A(h - h_p)^m \quad (1)$$

where h_p is the value of h corresponding to complete unloading, i.e. $F = 0$, and A and m are fitting parameters. The contact stiffness S at the maximum load F_{max} is then

$$S = mA(h_{max} - h_p)^{m-1} \quad (2)$$

where h_{max} is the value of h corresponding to F_{max} . Subsequently, the contact depth h_c was determined as

$$h_c = h_{max} - \epsilon F_{max}/S \quad (3)$$

For reasons that will become clear later, the value of the geometrical parameter ϵ in the last expression was not adjusted on the basis of the calculated m value via the common formula $\epsilon = \epsilon(m)$ provided in e.g. [33], but it was instead preset to 0.75, which is a value appropriate for most materials [33]. The value of h_c from equation (3) was employed to find the projected contact area A , where the function $A = A(h_c)$ was determined via calibration of the nano-indentation instrument, and eventually the reduced Young's modulus E^* was estimated as

$$E^* = \frac{1}{2} \frac{\sqrt{\pi} S}{1.05 \sqrt{A}} \quad (4)$$

It is worth remarking that E^* is directly connected to the Young's modulus and Poisson's ratio of the material being indented (denoted by E and ν) and to those of the material the indenter is made of (denoted by E_i and ν_i) by the formula

$$\frac{1}{E^*} = \frac{1 - \nu^2}{E} + \frac{1 - \nu_i^2}{E_i} \quad (5)$$

As E_i is usually $\gg E$, the influence of the second term on the right-hand-side of equation (5) is normally negligible.



Figure 2: μ CT scan of a small volume of the DCI sample, with indication of the nodule selected for nano-indentation analysis (red arrows). (a) Appearance of the part of the scanning volume exposed to the sample surface. (b) Sub-surface morphology of the nodules visible in (a). (c) Close-up view of the selected nodule.



Figure 3: Setup of the nano-indentation tests. (a) Selected nodule. (b) Close-up with indication of the s- and t-axis along which the two series of nano-indentations were made.

3. Results

3.1 Shape of the load vs. penetration curves

The load versus penetration curves obtained from the indents made along the s- and t-axis are reported in Figure 4 (a) and (b) respectively. Simple visual inspection indicates that significant differences exist in the shape of the curves, in connection with all of the three stages of loading, holding and unloading. To analyze these differences in more quantitative terms, the maximum indenter penetration h_{max} and the permanent indenter penetration h_p are extracted from each curve and compared.

(a) (b)

Figure 4: Load vs. penetration curves obtained from the indents performed along (a) the s-axis and (b) along the t-axis. The axial coordinate of each indent (in μm) is reported in the legend.

Figure 5 (a) shows h_{max} as a function of the position along both axes. It can be seen that the maximum value recorded is $\approx 0.5 \mu\text{m}$. On the basis of this value, the ASTM standard E2546 – 15 “Standard Practice for Instrumented Indentation Testing” [34] recommends a minimum distance of $8.4 \mu\text{m}$ between each indent and features like other indents or material interfaces. As $8.4 \mu\text{m} < 10 \mu\text{m}$, the distance selected in this work between consecutive indents and between indents and the nodule-matrix boundary can be considered appropriate. With respect to the spatial variation of h_{max} , Figure 5 (a) reveals that a factor 2 fluctuation exists, implying that the material resistance against penetration is apparently very scattered. However, the scatter of h_{max} is not randomly distributed along the axes. On the contrary, it appears that h_{max} follows some sort of predefined pattern, which is roughly symmetric for the indents made along the t-axis. To check this qualitative impression, a paired t-test [35] is performed to analyze, on statistical basis, the mean value of the difference in h_{max} recorded between pairs of indents located at the same distance from the origin of the axis, i.e. characterized by opposite values of the axial coordinate. The basic

idea is that no difference should exist if the pattern was symmetric. The outcome of the paired t-test is reported in Table 2 and shows that, for the t-axis, a P-value of 0.149 is obtained. This high P-value means that the hypothesis that h_{max} follows a symmetric pattern cannot be rejected at any reasonable significance level. Conversely, Table 2 indicates that, if the same type of test is performed using data from the indents along the s-axis, a much smaller P-value of 0.028 is obtained. For a standard confidence level of 95%, this leads to rejection of the hypothesis that the h_{max} pattern is symmetric. Thus, there is statistical evidence that the h_{max} pattern is symmetric along the t-axis and asymmetric along the s-axis.

Figure 5 (b) shows the variation of the ratio h_p/h_{max} instead, which provides a simple measure of the relative amount of plastic deformation occurring during the nano-indentation process [36]. Note that possible values lie within the interval [0, 1], where zero means that the tested material is perfectly elastic and one means that the tested material exhibits a perfectly plastic response, with no elastic spring-back. Contrary to Figure 5 (a), no clear pattern is distinguishable in Figure 5 (b), as the scatter in h_p/h_{max} seems to be distributed more uniformly and within a more restricted range of values. Concerning this last point, all but two values lie in the interval [0.55, 0.80], which include the values of ≈ 0.60 and ≈ 0.55 that can be estimated from the two F vs. h curves for the nodules reported in [23] and [37] respectively. In addition, comparison with Table 3 reveals that the h_p/h_{max} values calculated in the present work are also fairly close to those characteristic of other non-metallic materials like e.g. soda-lime glass and sapphire.

(a)

(b)

Figure 5: Shape parameters of the load vs. penetration curves. (a) Maximum indenter penetration as a function of the position along the s- and t-axis. (b) Ratio between permanent and maximum indenter penetration as a function of the position along the s- and t-axis.

Table 2: Outcome of the paired t-test used to check the symmetry of the maximum indenter penetration pattern of Figure 5 (a).

Axis	Variable	N indents	Mean (μm)	StDev (μm)	Paired t-test	
					t-value	P-value
s-axis	h_{max}^{s-}	6	398.4	79.2	3.05	0.028
	h_{max}^{s+}	6	273.2	53.7		
t-axis	h_{max}^{t-}	8	324.9	63.2	1.62	0.149
	h_{max}^{t+}	8	293.7	41.8		

Table 3: Typical parameters of load vs. penetration curves relative to common materials. Data from [21].

Material	Young's modulus [GPa]	h_p/h_{max}	m	n
Aluminum	74.8	≈ 1	1.38	2.63
Quartz	88.2	≈ 0.50	1.43	2.33
Soda-lime glass	69.4	≈ 0.65	1.37	2.70
Sapphire	310.8	≈ 0.62	1.47	2.13
Fused silica	69.6	≈ 0.55	1.25	4.00
Tungsten	320.4	≈ 1	1.51	1.96

3.2 Young's modulus calculated using the Oliver & Pharr method

Figure 6 (a) and (b) show the values of the exponent m calculated by fitting either the upper 40% or the upper 90% of the unloading data with equation (1). It can be observed that the choice of the fitting range leads to a variation in the results which is, on average, in the order of $\approx 30\%$. In this respect, it should also be noted that the present values of m are significantly larger than those reported for all the materials listed in Table 3, no matter the choice of the fitting range.

(a)

(b)

Figure 6: Values of the m exponent that best fit the unloading data according to equation (1), as a function of the position along the s- and t-axis. In (a) the upper 40% of the unloading data is used in the fitting procedure, whereas in (b) the upper 90% is used.

The values of the reduced Young's modulus calculated for both choices of the fitting range are presented in Figure 7 (a) and (b). The non-uniform scatter of the results seems to indicate that, similarly to h_{max} , E^* follows some sort of predefined pattern, which is symmetric along the t-axis and asymmetric along the s-axis. The results of a statistical analysis based on the same paired t-test that was used to analyze the h_{max} data support this speculation. Indeed, as reported in Table 4 and Table 5, very high P-values – close to 0.8 – are obtained from the data along the t-axis, whereas small P-values – 0.020 and 0.035 – are calculated from the data along the s-axis. As explained in the previous section, for a standard confidence level of 95% these values indicate symmetry along the t-axis and asymmetry along the s-axis. In addition to possessing the same symmetrical features, closer comparison between Figure 7 and Figure 5 (a) suggests that the pattern of E^* is, to some extent, complimentary to that of h_{max} . That is, at the coordinate where h_{max} attains its maximum, E^* attains its minimum and vice-versa. The choice of the fitting range does not seem to affect significantly the shape of the E^* pattern. Indeed, all the E^* values seem to be affected by an equal relative change in magnitude when the fitting range switches from 40% to 90%. However, such change in magnitude is actually very pronounced, as demonstrated by the fact that the mean values of E^* are 19.3 ± 7.6 GPa and 13.1 ± 4.7 GPa for a fitting range of 40% and 90%, respectively (uncertainty expressed as one standard deviation). This is likely a consequence of the strong dependence of m on the fitting range, pointed out in the previous paragraph, which inevitably impacts the calculation of the contact stiffness in equation (2) and thereby the determination of the reduced Young's modulus. Concerning comparison with previous works in the field, Pradhan *et al.* and Fernandino *et al.* determined the values of Young's modulus listed in Table 1 by assuming that the Poisson's ratio of the nodules was 0.126 and 0.26, respectively. This implies that, according to equation (10) and neglecting the contribution from the indenter stiffness, the values of E^* they derived with the Oliver & Pharr method were $\approx 29 \pm 9$ GPa and $\approx 16 \pm 4$ GPa, respectively. Both values are in agreement with the present estimate of 16.2 ± 7.0 GPa, which represents the average of the mean values of E^* found for the two choices of the fitting range.

(a)

(b)

Figure 7: Reduced Young's modulus as a function of the position along the s- and t-axis. Values are calculated according to the Oliver & Pharr method, where the m exponent is determined by fitting either (a) the upper 40% or (b) the upper 90% of the unloading data.

Table 4: Outcome of the paired t-test used to check the symmetry of the reduced Young's modulus data of Figure 7 (a).

Axis	Variable	N indents	Mean (GPa)	StDev (GPa)	Paired t-test	
					t-value	P-value
s-axis	E_{s-}^*	6	11.8	3.1	3.38	0.020
	E_{s+}^*	6	23.8	7.6		
t-axis	E_{t-}^*	8	20.1	9.8	0.25	0.809
	E_{t+}^*	8	21.0	2.7		

Table 5: Outcome of the paired t-test used to check the symmetry of the reduced Young's modulus data of Figure 7 (b).

Axis	Variable	N indents	Mean (GPa)	StDev (GPa)	Paired t-test	
					t-value	P-value
s-axis	E_{s-}^*	6	8.8	2.7	2.88	0.035
	E_{s+}^*	6	14.7	3.9		
t-axis	E_{t-}^*	8	14.6	6.5	-0.27	0.796
	E_{t+}^*	8	13.9	2.4		

4. Discussion

4.1 Interpretation of the results on the basis of the nodule structure

A primary outcome of the analysis of section 3.1 is that the pattern of h_{max} – symmetric along the t-axis but not along the s-axis – is hardly explainable on the basis of the statistical fluctuation of the results due to the experimental error. This indicates that the influence of the internal structure of the nodule is not negligible in the present context. Indeed, if it was, meaning that the nodule could be considered isotropic and homogeneous, the spatial position and orientation of each indent would be irrelevant, as long as it is made at sufficient distance from the nodule-matrix interface.

To provide a qualitative explanation for why the pattern of h_{max} exhibits symmetric features, it is useful to introduce a simplified model of the internal structure of the nodule. As explained in the introduction and shown in Figure 1, each particle consists of conical sectors radiating from its center, which are formed by graphite platelets stacked one upon the other. The number of conical sectors is typically fairly large, with rough estimates placing it between 56 and 225 [11]. If assumed that this number is *infinitely* large, the nodule can be thought of as a particle with spherical symmetry, as the vector normal to the graphite platelets (the c-axis in Figure 1) becomes radially oriented at any point inside the nodule. This means that the particle can be considered as made by many concentric shells, each representing a single layer of graphite. The equatorial cross-section of such a simplified model would then look like in Figure 8 (a), where the center of the nodule is individuated by the origin of the x-y-z coordinate system and the concentric circles marked with black solid lines represent the graphite layers. At this point, one can assume that the exposed section of the particle highlighted in Figure 2 and Figure 3, onto which the nano-indentation tests were made, is equivalent to the cross-section obtained by sectioning the model with a plane which is normal to the z-axis and intersects the latter at $z = w$. Figure 8 (b) shows a schematic of such cross-section, where, for convenience, it is assumed that the s-axis and t-axis are parallel to the x-axis and y-axis, respectively. On the same figure, four different Berkovich indenters are also represented, which are denoted by I1, ..., I4. All these indenters are sketched with the same orientation, which corresponds to the one of the

real indenter used for making the nano-indentation tests. By comparing the orientation of the indenters to the underlying orientation of the graphite layers, it is not difficult to realize that the position of I3 *is perfectly equivalent* to that of I4 – they simply represent mirrored configurations. Conversely, the position of I1 *is not equivalent* to that of I2 – they would be equivalent if either I1 or I2 was rotated 180° about the z-axis. Hence, according to the schematic of Figure 8 (b), positions symmetric about the x-axis are equivalent, whereas positions symmetric about the y-axis are not. This provides a simple explanation for the symmetry (resp. asymmetry) of the pattern of h_{max} and E^* experimentally observed along the t-axis (resp. the s-axis).

(a) (b)

Figure 8: Simplified spherical model used to analyze the interaction between the Berkovich indenter and the graphite platelets forming the nodule. (a) 3D view of the equatorial cross-section of the model (b) Top-view of the x-y cross-section at $z = w$.

The simplified model of Figure 8 can also be used to attempt a justification for the variation of h_{max} with the s- and t-coordinate. Indeed, according to the discussion reported in the introduction, the graphite platelets can be separated easily along the basal plane by the action of a sharp indenter. As h_{max} represents the local resistance of the material against penetration, it follows that a high value of h_{max} will be recorded when the graphite platelets below the indenter are oriented in a way that promotes sliding of the indenter along the basal plane. In the present work, it is assumed that this condition is fulfilled when there is a high level of alignment between the basal plane and one of the three faces of the indenter. Since the orientation of the indenter faces is fixed and the orientation of the graphite basal plane can be approximated by the model of Figure 8, it is possible to formulate an alignment function f that, if the previous assumption holds, should describe qualitatively the dependence of h_{max} on the spatial coordinates.

The alignment function is constructed in the following way. As shown in Figure 8 (b), the orientation of the three indenter faces can be described by three normal vectors \mathbf{n}_{Y+} , \mathbf{n}_{Y-}

and \mathbf{n}_{X-} . On the basis of the standard Berkovich geometry with face angle of 65.27° , it is possible to write their components in the x-y-z coordinate system as

$$\mathbf{n}_{Y+} = \begin{bmatrix} 0.209 \\ 0.362 \\ -0.909 \end{bmatrix}, \quad \mathbf{n}_{Y-} = \begin{bmatrix} 0.209 \\ -0.362 \\ -0.909 \end{bmatrix}, \quad \mathbf{n}_{X-} = \begin{bmatrix} -0.418 \\ 0 \\ -0.909 \end{bmatrix} \quad (6)$$

Similarly, the orientation of the graphite basal plane can be described by its normal \mathbf{n}_G , which, according to the simplified model of the nodule, can be considered radially-oriented pointwise. Therefore, the components of \mathbf{n}_G can be expressed as [38]

$$\mathbf{n}_G = \begin{bmatrix} \sin(\theta)\cos(\phi) \\ \sin(\theta)\sin(\phi) \\ \cos(\theta) \end{bmatrix}, \quad \begin{cases} \theta = \arccos\left(\frac{z}{\sqrt{x^2 + y^2 + z^2}}\right) \\ \phi = \arctan(y/x) \end{cases} \quad (7)$$

where the inverse tangent function must be suitably defined to take the correct quadrant of (x, y) into account, so that its range is $[-\pi, \pi]$. As the vectors \mathbf{n}_{Y+} , \mathbf{n}_{Y-} , \mathbf{n}_{X-} and \mathbf{n}_G have all unit length, the cosines of the angles γ_{Y+} , γ_{Y-} and γ_{X-} that the indenter faces form with the graphite basal plane are obtainable via the scalar products

$$\begin{aligned} \cos(\gamma_{Y+}) &= \mathbf{n}_G \cdot \mathbf{n}_{Y+} \\ \cos(\gamma_{Y-}) &= \mathbf{n}_G \cdot \mathbf{n}_{Y-} \\ \cos(\gamma_{X-}) &= \mathbf{n}_G \cdot \mathbf{n}_{X-} \end{aligned} \quad (8)$$

The alignment function can then be defined as the maximum of the absolute values of the angle cosines:

$$f(x, y, z) = \max[|\cos(\gamma_{Y+})|, |\cos(\gamma_{Y-})|, |\cos(\gamma_{X-})|] \quad (9)$$

This definition implies that $f(x, y, z)$ is always positive and attains its maximum – one – when one of the indenter faces is perfectly aligned with the graphite basal plane.

As an example, Figure 9 (a) shows the x-z cut-view of a nodule sliced by a plane perpendicular to the z-axis at a distance from its center equal to 50% the nodule radius R. It is assumed that a series of nano-indentations is made on the sectioned surface along a path parallel to the x-axis. Figure 9 (b) shows the variation of the angle cosines with x, assuming that the path lies on the x-z plane. Note that, due to symmetry, the curves describing the cosines of γ_{Y+} and γ_{Y-} overlap. Figure 9 (c) shows the variation of the same angle cosines, but assuming that the path is now located at a distance from the x-z plane equal to 50% R. This time, the cosines of γ_{Y+} and γ_{Y-} are no longer equal, due to the path offset in the y-

direction. It is worth observing that, in graphical terms, $f(x, y, z)$ can be interpreted as the curve that provides the upper bound to the plots of the three angle cosines.

(a) (b) (c)

Figure 9: Example of application of the formulas (10). (a) Schematic x-z cut-view of a nodule sliced perpendicularly to the z-axis. (b) Variation of the indenter face - basal plane angle cosines along a path parallel to the x-axis and lying on the x-z plane. (c) The same as in (b), but assuming that the path is located at a distance from the x-z plane equal to 50% the nodule radius R .

In order to compare the shape of the alignment function to the pattern of h_{max} , four geometrical parameters are needed: the radius of the nodule R , the z-coordinate w of the sample surface, the x-coordinate u of the t-axis and the y-coordinate v of the s-axis. Note that the last three parameters are simply related to the positioning of the s- and t-axis with respect to the nodule center. Estimates for R and w are determined in two steps, assuming that the nodule highlighted in Figure 2 and Figure 3 can be treated as a spherical cap. First, the distance $d = R + w$ between the sample surface and the deepest point of the nodule is estimated from the μ CT scan. Then, the radius of the circular section exposed to the surface, $r = (R^2 - w^2)^{1/2}$, is determined as the average side length of the black dashed rectangle depicted in Figure 3 (b). By solving the resulting system of two equations and two unknowns, it is found that $R \approx 109 \mu m$ and $w \approx 58 \mu m$. To calculate the other two parameters, it is assumed that the center of the same rectangle represents the projection of the nodule center onto the sample surface. By combining this with the absolute coordinates of the s- and t-axis provided by the nano-indentation instrument, it is found that $u \approx -5 \mu m$ and $v \approx -25 \mu m$. It is worth emphasizing that, on the basis of the present estimates of R and w , a value $33.1 \mu m$ is obtained [39] for the ratio between volume and surface area of the spherical cap representing the nodule. This is only 13% higher than the ratio calculated from μ CT, meaning that the spherical cap approximation is quite realistic.

Figure 10 compares the pattern of h_{max} recorded experimentally to that predicted by the alignment function, equation (9), assuming that the geometrical parameters determined in the previous paragraph apply. Good agreement can be observed along the s-axis as well as along the t-axis. To visualize the effect of the uncertainty on the geometrical parameters on the results, Figure 11 shows how the predicted pattern is affected by a variation of $\pm 10 \mu\text{m}$ in the value of w . It is seen that w acts as a sort of scaling factor, but does not change the shape of the predicted pattern. Figure 12 (a) and (b) shows, instead, that when the values of u and v are modified in the interval $\pm 10 \mu\text{m}$, some shape changes occur. Nevertheless, these are quite limited in magnitude, so that the overall pattern remains similar to the one recorded experimentally. It can then be concluded that the alignment function provides a realistic qualitative prediction of how the resistance against penetration varies in space as a consequence of the internal structure of the particle. To the authors' best knowledge, this result constitutes the first direct proof of the existence of a link between structure and mechanical properties of the nodules in DCIs.

To conclude this section, it has to be pointed out that some caution is, in principle, necessary, as the present conclusions are based on the indentation of one single graphite nodule. However, it is also worth emphasizing that such nodule was carefully selected via μCT analysis to have representative shape and size. Moreover, investigations [25–30] made on different nodules have shown that the internal structure is always consistent with the schematic of Figure 1, i.e. every nodule is formed by conical sectors which propagate radially from its center. As a consequence, there appear to be no reasons to presume that the same analysis performed on different nodules would lead to different results.

(a)

(b)

Figure 10: Comparison between the pattern predicted by the alignment function, equation (9), and the experimental data in terms of maximum indenter penetration. (a) Indents along the s-axis, (b) indents along the t-axis.

(a) (b)

Figure 11: Effect of the uncertainty on the w parameter on the pattern predicted by the alignment function, equation (9). (a) Pattern along the s-axis. (b) Pattern along the t-axis.

(a) (b)

Figure 12: Effect of the uncertainty on the u and v parameters on the pattern predicted by the alignment function, equation (9). (a) Effect of v uncertainty on the pattern along the s-axis. (b) Effect of u uncertainty on the pattern along the t-axis.

4.2 Applicability of the Oliver & Pharr method

In the introduction, it was pointed out that the anisotropy associated with the non-random orientation of the graphite platelets inside the nodule could generate inconsistencies in the application of the Oliver & Pharr method. Concerning this, an unusual element detected in the present work is the very high values of the fitting exponent m , which are significantly larger than those reported for other materials.

As explained in detail elsewhere [33,36], the shape of the unloading part of the F vs. h curve, quantified by m , can be related to the shape of the so-called equivalent indenter (EI), which is a concept implicitly used in the equations of the Oliver & Pharr method. Indeed, the EI approach justifies modeling the unloading stage, which involves contact between the indenter and the plastically-deformed sample surface, by means of an elastic solution valid for contact with a perfectly flat surface. Thus, the EI concept allows replacing the physical contact geometry with an equivalent one, which is easier to analyze mathematically. Figure

13 (a) shows how these two geometries are connected to each other. According to [33,36], the Oliver & Pharr method assumes that the EI is axisymmetric and its profile is described by a power-law expression of the type $y = ax^n$. Under this assumption, the two exponents m and n are related to each other by the expression

$$n = 1/(m - 1) \quad (10)$$

The importance of equation (10) lies in the fact that it is routinely used to calculate n from the value of m determined by fitting the unloading data. On the basis of n , the parameter ϵ entering equation (3) is found via the function $\epsilon = \epsilon(n)$, which comes from the elastic solution to the equivalent contact problem.

In the present work, the calculated values of m are often greater than 2, see Figure 6. However, close inspection of equation (10) reveals that $m > 2$ implies $n < 1$. This means that the profile of the EI degenerates into a non-convex shape, see Figure 13 (b), for which the elastic solution the Oliver & Pharr method is based on is not valid anymore. As a consequence, the values delivered by the function $\epsilon = \epsilon(n)$ become meaningless and one might reasonably become skeptical about the values of E^* calculated with this method. On the other hand, a recent re-examination of the Oliver & Pharr equations demonstrated that, when a consistent relation between projected contact area A and contact depth h_c is invoked, the method can be seen as based on an EI which is conical in shape and whose semi-apical angle α is a function of ϵ and of the ratio h_p/h_{max} [40]. Remarkably, within this frame ϵ is just a parameter which controls α and it is connected neither to the fitting exponent m nor to the power-law shape of the EI, because the latter is assumed conical a priori. Moreover, the accuracy of the method is explainable by the choice of the function $\alpha = \alpha(\epsilon, h_p/h_{max})$, which, for common values of ϵ , has a very clear physical interpretation. All in all, this means that if ϵ is preset to a standard value of 0.75 as done in the present analysis – and not calculated via equation (10) and the relation $\epsilon = \epsilon(n)$ reported in the literature – one does not need to worry about inconsistencies due to values of m greater than 2.

(a)

(b)

Figure 13: Equivalent indenter analogy assuming a power-law profile of the type $y = ax^n$. (a) Case $n > 1$. (b) Case $n < 1$.

In conclusion, it can be stated that the unusual slope of the unloading part of the F vs. h curves does not invalidate the results of section 3.2. On the other hand, due to the non-negligible mechanical anisotropy revealed in the present investigation, the calculated mean value of E^* should be considered only as indicative of a sort of “averaged” elastic stiffness. Caution should then be used when assessing the elastic response of the entire nodule just on the basis of the former quantity, as complex anisotropic effects associated with the non-random orientation of the graphite platelets can be expected.

5. Conclusions

In the present work nano-indentation tests were performed on the cross-section of a graphite nodule in a DCI sample. First, the sub-surface morphology of the nodule was characterized via μ CT to evaluate the 3D geometrical features of the particle. Then, two series of nano-indents were made on the nodule cross-section along two axes perpendicular to each other. On the basis of the recorded load vs. penetration curves, the spatial variation of the maximum indenter penetration h_{max} , which describes the mechanical resistance of the material against penetration, was determined. The spatial variation of the reduced Young’s modulus was calculated as well by means of the Oliver & Pharr method. The

results were analyzed by means of statistical techniques and interpreted on the basis of the internal structure of the nodule. The main findings can be summarized as follows:

1. The recorded pattern of h_{max} presents features which, statistically, are not explainable with the experimental error. Conversely, they can be justified in a natural manner by a model which takes into account the geometrical interaction between the indenter and the local orientation of the graphite platelets forming the nodule. To the authors' best knowledge, this result constitutes the first direct proof of the existence of a link between internal structure and mechanical properties of the nodules.
2. The local mechanical anisotropy revealed in the present work has a significant impact on the shape of the nano-indentation curves. This does not invalidate the application of the Oliver & Pharr method, as long as the parameter ϵ is fixed and not calculated from the shape of the unloading part of the curves. Nevertheless, the calculated mean value of E^* can only be seen as indicative of a sort of "averaged" elastic stiffness. Caution should be used when assessing the elastic response of the entire nodule just on the basis of this parameter, as complex anisotropic effects associated with the non-random orientation of the graphite platelets can be expected.

Acknowledgements

This work has been supported by the Strategic Research Center "REWIND - Knowledge based engineering for improved reliability of critical wind turbine components", Danish Research Council for Strategic Research, grant no. 10-093966. Vestas Wind Systems A/S is gratefully acknowledged for providing the DCI used in the nano-indentation experiments.

Authors' contribution

S. Fæster prepared the DCI sample and performed the μ CT scans. G. Winther carried out the nano-indentation tests. T. Andriollo analyzed the data and developed the theoretical model. All authors discussed the results together. T. Andriollo wrote the article, which all authors approved.

References

- [1] 50th Census of World Casting Production, *Mod. Cast. - A Publ. Am. Foundry Soc.* (2016) 25–29.
- [2] C. Labrecque, M. Gagne, Review ductile iron: 50 years of continuous development, *Can. Metall. Q.* 37 (1998) 343–378.
- [3] N.S. Tiedje, Solidification, processing and properties of ductile cast iron, *Mater. Sci. Technol.* 26 (2010) 505–514. doi:10.1179/026708310X12668415533649.
- [4] J.R. Keough, K.L. Hayrynen, G.L. Pioszak, Designing with Austempered Ductile Iron (ADI), *Trans. Am. Foundry Soc.* 118 (2010) 503–517.
- [5] M.J. Dong, B. Tie, A.S. Béranger, C. Prioul, D. François, Damage Effect on the Fracture Toughness of Nodular Cast Iron, *Adv. Mater. Res.* 4–5 (1997) 181–188. doi:10.4028/www.scientific.net/AMR.4-5.181.
- [6] C. Berdin, M.J. Dong, C. Prioul, Local approach of damage and fracture toughness for nodular cast iron, *Eng. Fract. Mech.* 68 (2001) 1107–1117.
- [7] L. Collini, A. Pironi, Fatigue crack growth analysis in porous ductile cast iron microstructure, *Int. J. Fatigue.* 62 (2014) 258–265. doi:10.1016/j.ijfatigue.2013.06.020.
- [8] G. Hütter, L. Zybelle, M. Kuna, Micromechanical modeling of crack propagation in nodular cast iron with competing ductile and cleavage failure, *Eng. Fract. Mech.* 147 (2015) 388–397. doi:10.1016/j.engfracmech.2015.06.039.
- [9] K. Salomonsson, J. Olofsson, Analysis of Localized Plastic Strain in Heterogeneous Cast Iron Microstructures Using 3D Finite Element Simulations, in: P. Mason, C.R. Fisher, R. Glamm, M. V Manuel, G.J. Schmitz, A.K. Singh, et al. (Eds.), *Proc. 4th World Congr. Integr. Comput. Mater. Eng. (ICME 2017)*, Springer International Publishing, Cham, 2017: pp. 217–225. doi:10.1007/978-3-319-57864-4_20.
- [10] D.O. Fernandez, A.P. Cislino, S. Toro, P.J. Sanchez, Multi-scale analysis of the early damage mechanics of ferritized ductile iron, *Int. J. Fract.* (2017). doi:10.1007/s10704-017-0215-1.
- [11] T. Andriollo, K. Hellström, M.R. Sonne, J. Thorborg, N. Tiedje, J. Hattel, Uncovering the local inelastic interactions during manufacture of ductile cast iron: How the substructure of the graphite particles can induce residual stress concentrations in the matrix, *J. Mech. Phys. Solids.* 111 (2018) 333–357. doi:10.1016/j.jmps.2017.11.005.
- [12] G. Iannitti, A. Ruggiero, N. Bonora, S. Masaggia, F. Veneri, Micromechanical modelling of constitutive behavior of austempered ductile iron (ADI) at high strain rate, *Theor. Appl. Fract. Mech.* (2017). doi:10.1016/j.tafmec.2017.05.007.
- [13] G. Hütter, L. Zybelle, M. Kuna, Micromechanisms of fracture in nodular cast iron: From experimental findings towards modeling strategies – A review, *Eng. Fract. Mech.* 144 (2015) 118–141. doi:10.1016/j.engfracmech.2015.06.042.
- [14] T. Andriollo, J. Hattel, On the isotropic elastic constants of graphite nodules in ductile cast iron: Analytical and numerical micromechanical investigations, *Mech. Mater.* 96 (2016) 138–150. doi:10.1016/j.mechmat.2016.02.007.
- [15] T. Andriollo, J. Thorborg, J. Hattel, Modeling the elastic behavior of ductile cast iron including anisotropy in the graphite nodules, *Int. J. Solids Struct.* (2016).
- [16] Y.B. Zhang, T. Andriollo, S. Fæster, W. Liu, J. Hattel, R.I. Barabash, Three-dimensional local residual stress and orientation gradients near graphite nodules in ductile cast iron, *Acta Mater.* 121 (2016) 173–180. doi:10.1016/j.actamat.2016.09.009.
- [17] W. Baer, Performance of Modern DCI Materials – Investigation of Microstructural, Temperature and Loading Rate Effects on Mechanical and Fracture Mechanical Properties, *Mater. Sci. Forum.* 783–786 (2014) 2244–2249. doi:10.4028/www.scientific.net/MSF.783-786.2244.
- [18] V. Di Cocco, F. Iacoviello, A. Rossi, D. Iacoviello, Macro and microscopical approach to the damaging micromechanisms analysis in a ferritic ductile cast iron, *Theor. Appl. Fract. Mech.* 69 (2014) 26–33. doi:10.1016/j.tafmec.2013.11.003.
- [19] D.O. Fernandez, R. Boeri, Study of the fracture of ferritic ductile cast iron under different loading conditions, *Fatigue Fract. Eng. Mater. Struct.* 38 (2015) 610–620. doi:10.1111/ffe.12266.
- [20] F. Iacoviello, V. Di Cocco, Influence of the graphite elements morphology on the fatigue crack

- propagation mechanisms in a ferritic ductile cast iron, *Eng. Fract. Mech.* (2016). doi:10.1016/j.engfracmech.2016.03.041.
- [21] W.C. Oliver, G.M. Pharr, An improved technique for determining hardness and elastic modulus using load and displacement sensing indentation experiments, *J. Mater. Res.* 7 (1992) 1564–1580.
- [22] P. Dierickx, C. Verdu, A. Reynaud, R. Fougères, A study of physico-chemical mechanisms responsible for damage of heat treated and as-cast ferritic spheroidal graphite cast irons, *Scr. Mater.* 34 (1996) 261–268. doi:10.1016/1359-6462(95)00496-3.
- [23] S.K. Pradhan, B.B. Nayak, S.S. Sahay, B.K. Mishra, Mechanical properties of graphite flakes and spherulites measured by nanoindentation, *Carbon N. Y.* 47 (2009) 2290–2292. doi:10.1016/j.carbon.2009.04.024.
- [24] N. Bonora, A. Ruggiero, Micromechanical modeling of ductile cast iron incorporating damage. Part I: Ferritic ductile cast iron, *Int. J. Solids Struct.* 42 (2005) 1401–1424. doi:10.1016/j.ijsolstr.2004.07.025.
- [25] B. Miao, K. Fang, W. Bian, G. Liu, On the microstructure of graphite spherulites in cast irons by TEM and HREM, *Acta Metall. Mater.* 38 (1990) 2167–2174. doi:10.1016/0956-7151(90)90084-T.
- [26] B. Miao, D.O. North Wood, W. Bian, K. Fang, M.H. Fan, Structure and growth of platelets in graphite spherulites in cast iron, *J. Mater. Sci.* 29 (1994) 255–261. doi:10.1007/BF00356601.
- [27] J.P. Monchoux, C. Verdu, G. Thollet, R. Fougères, A. Reynaud, Morphological changes of graphite spheroids during heat treatment of ductile cast irons, *Acta Mater.* 49 (2001) 4355–4362. doi:10.1016/S1359-6454(01)00230-0.
- [28] K. Theuwissen, M.-C. Lafont, L. Laffont, B. Viguier, J. Lacaze, Microstructural Characterization of Graphite Spheroids in Ductile Iron, *Trans. Indian Inst. Met.* 65 (2012) 627–631. doi:10.1007/s12666-012-0162-5.
- [29] K. Theuwissen, J. Lacaze, M. Véron, L. Laffont, Nano-scale orientation mapping of graphite in cast irons, *Mater. Charact.* 95 (2014) 187–191. doi:10.1016/j.matchar.2014.06.021.
- [30] K. Theuwissen, J. Lacaze, L. Laffont, Structure of graphite precipitates in cast iron, *Carbon N. Y.* 96 (2016) 1120–1128. doi:10.1016/j.carbon.2015.10.066.
- [31] A.E.H. Love, Bousinesq's problem for a rigid cone, *Q. J. Math. os-10* (1939) 161–175. doi:10.1093/qmath/os-10.1.161.
- [32] T. Andriollo, J. Thorborg, N. Tiedje, J. Hattel, A micro-mechanical analysis of thermo-elastic properties and local residual stresses in ductile iron based on a new anisotropic model for the graphite nodules, *Model. Simul. Mater. Sci. Eng.* 24 (2016) 055012(19pp). doi:10.1088/0965-0393/24/5/055012.
- [33] W.C. Oliver, G.M. Pharr, Measurement of hardness and elastic modulus by instrumented indentation: Advances in understanding and refinements to methodology, *J. Mater. Res.* 19 (2004) 3–20.
- [34] ASTM International, Standard E2546 – 15: Standard Practice for Instrumented Indentation Testing, (2015).
- [35] D.C. Montgomery, *Design and Analysis of Experiments*, 8th ed., John Wiley & Sons, 2012.
- [36] G.M. Pharr, A. Bolshakov, Understanding nanoindentation unloading curves, *J. Mater. Res.* 17 (2002) 2660–2671.
- [37] D.O. Fernandez, A.P. Cisilino, R.E. Boeri, Determination of effective elastic properties of ferritic ductile cast iron by computational homogenization, micrographs and microindentation tests, *Mech. Mater.* 83 (2015) 110–121. doi:10.1016/j.mechmat.2015.01.002.
- [38] A.F. Bower, *Vectors and Tensor Operations in Polar Coordinates*, (n.d.). <http://solidmechanics.org/text/AppendixD/AppendixD.htm> (accessed October 18, 2017).
- [39] E.W. Weisstein, Spherical Cap, *MathWorld--A Wolfram Web Resour.* (2018). <http://mathworld.wolfram.com/SphericalCap.html> (accessed March 6, 2018).
- [40] T. Andriollo, J. Thorborg, J. Hattel, Analysis of the equivalent indenter concept used to extract Young's modulus from a nano-indentation test: some new insights into the Oliver–Pharr method, *Model. Simul. Mater. Sci. Eng.* 25 (2017) 45004(22pp). doi:10.1088/1361-651X/aa6831.

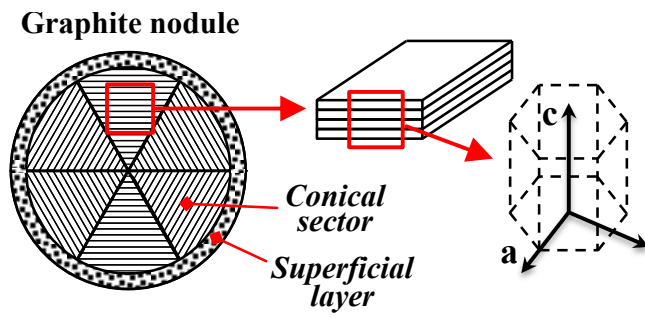


FIG.1

ACCEPTED MANUSCRIPT

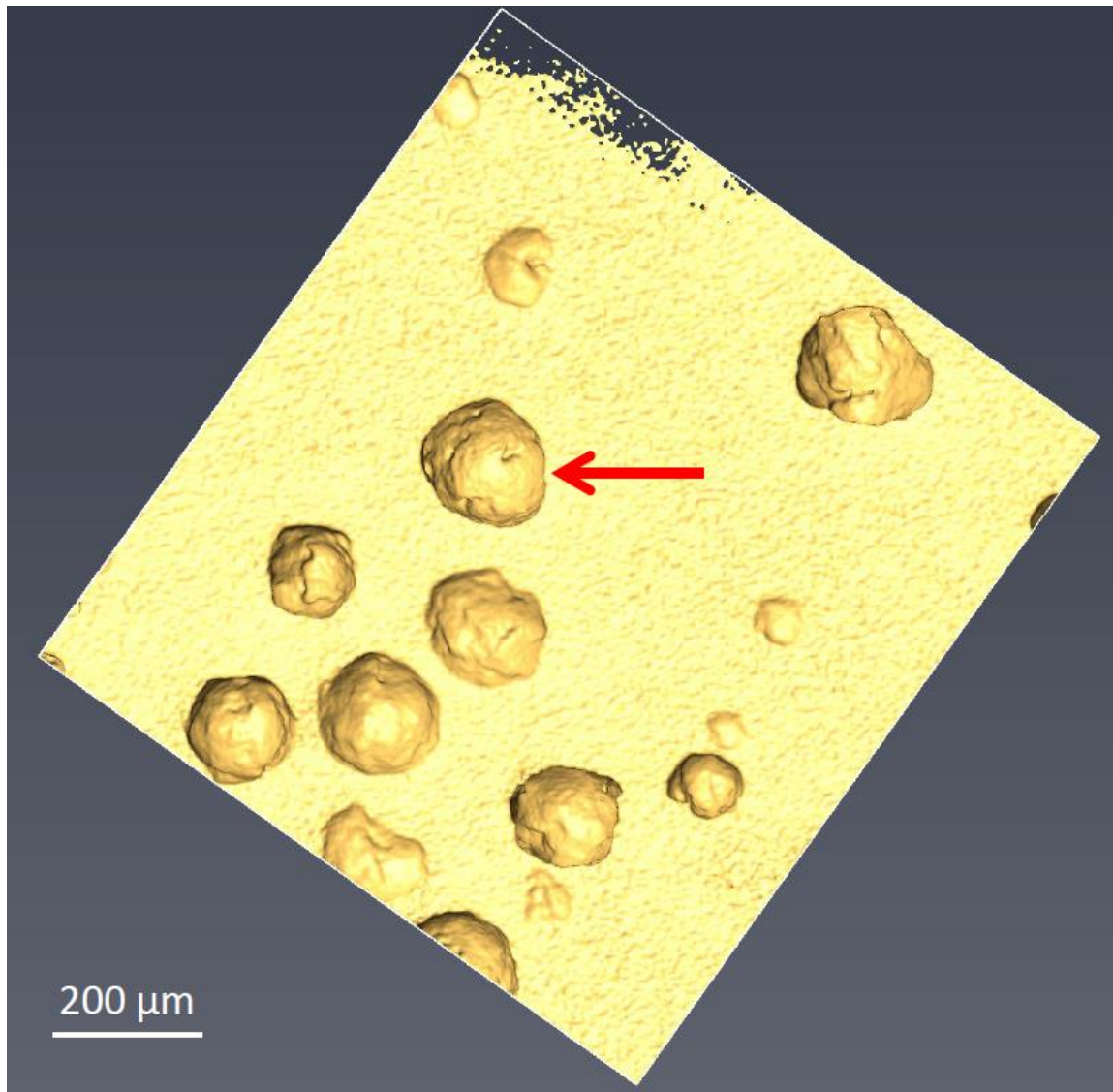


FIG.2(A)

ACCEPTED

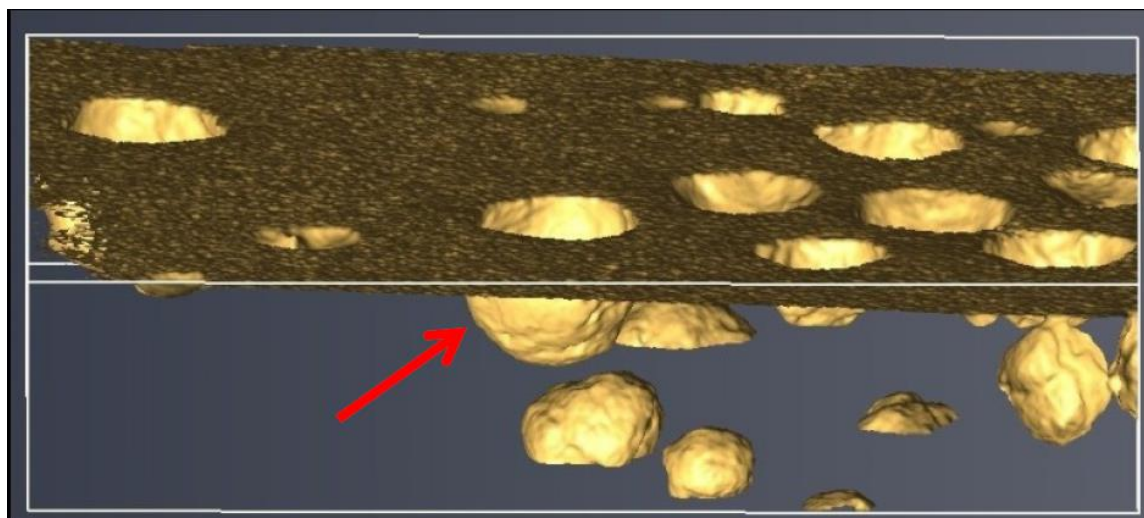


FIG.2(B)

ACCEPTED MANUSCRIPT

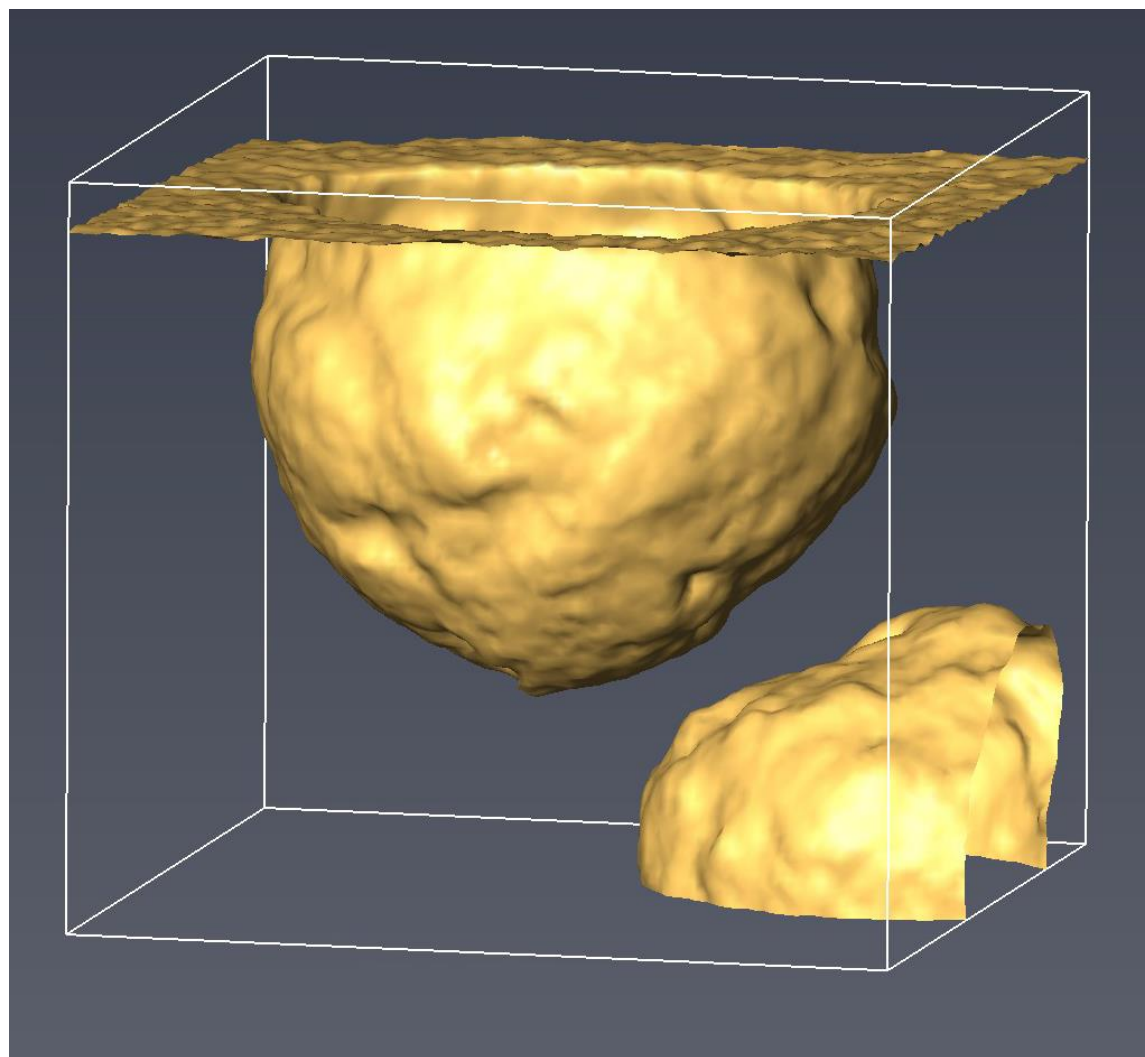


FIG.2(C)

ACCEPTED

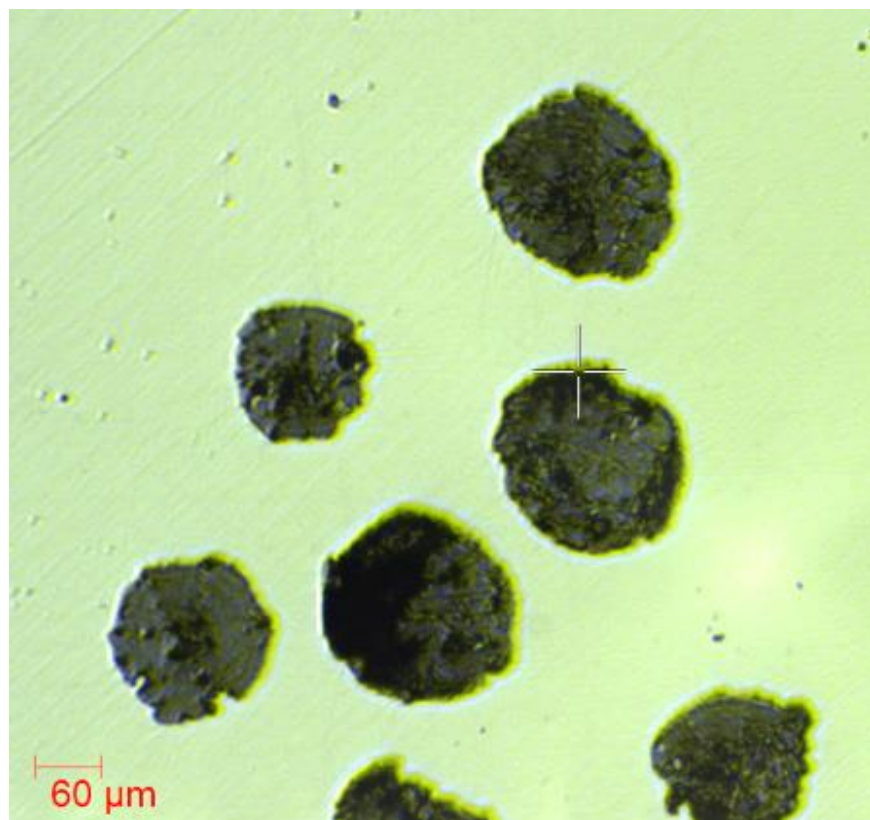


FIG.3(A)

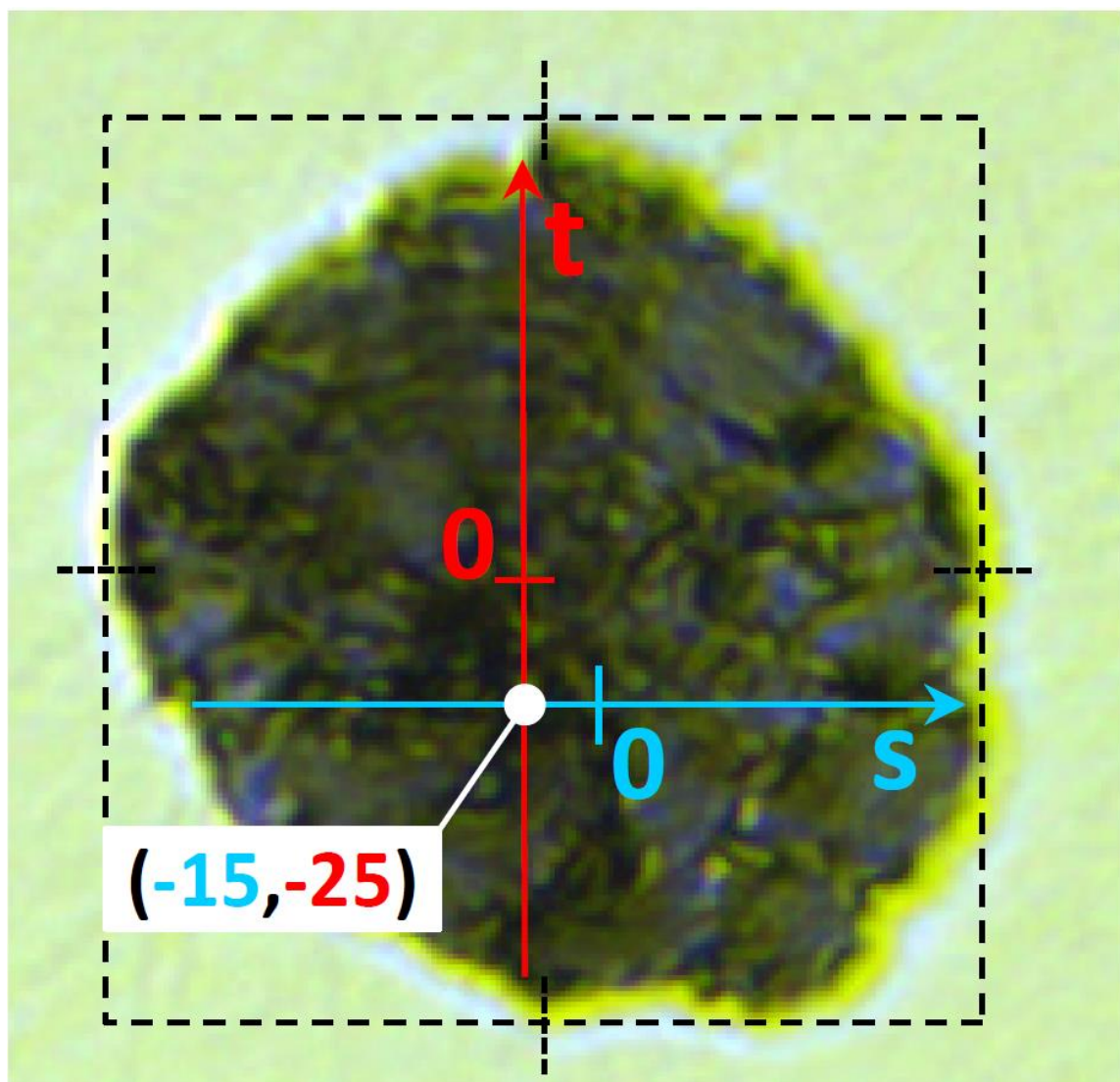


FIG.3(B)

ACCEPTED

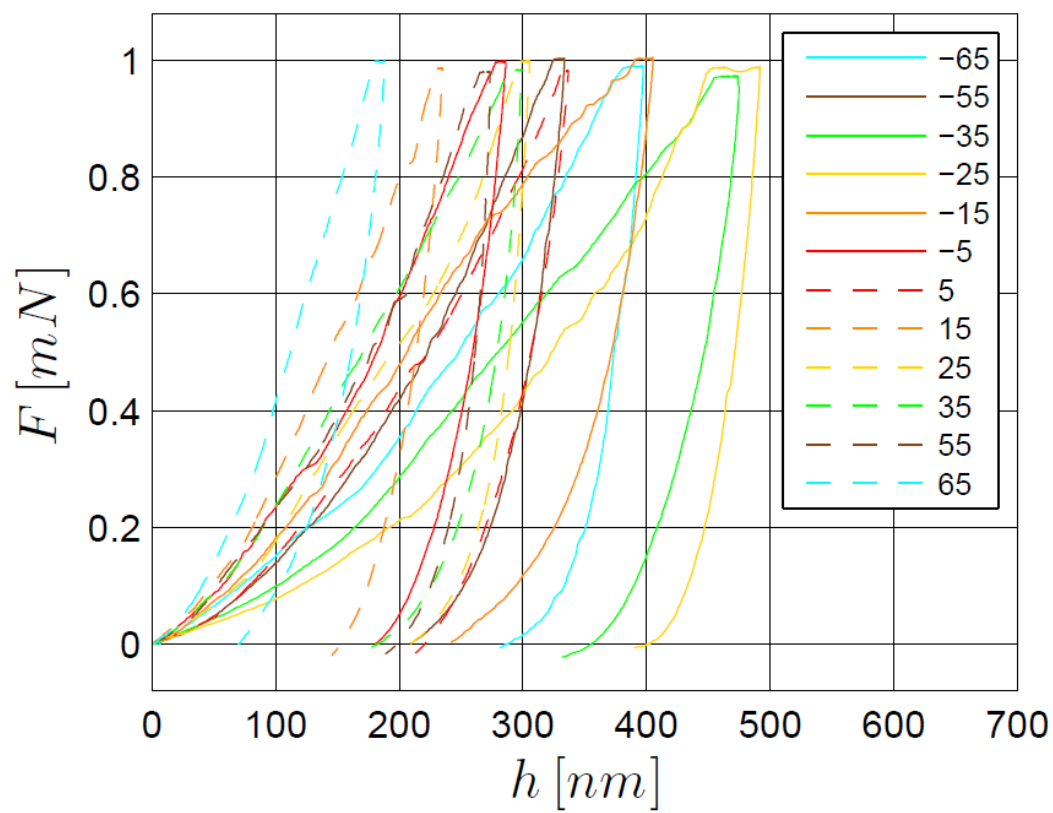


FIG.4(A)

ACCEPTED

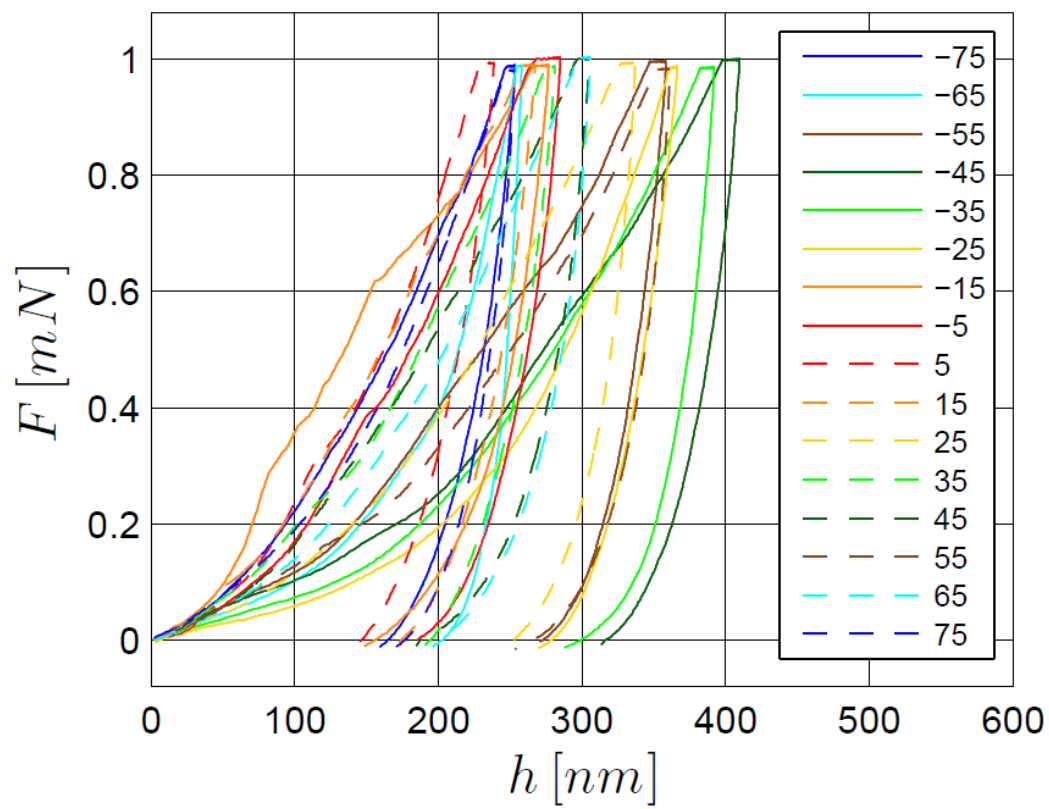


FIG.4(B)

ACCEPTED MANUSCRIPT

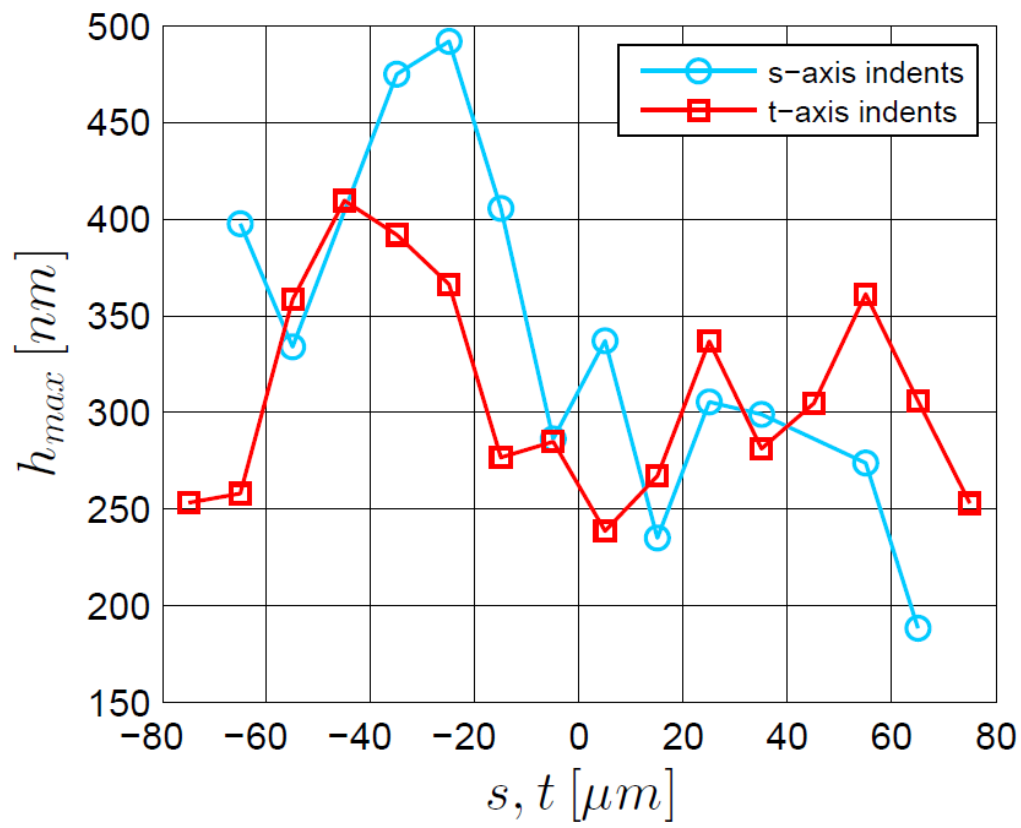


FIG.5(A)

ACCEPTED

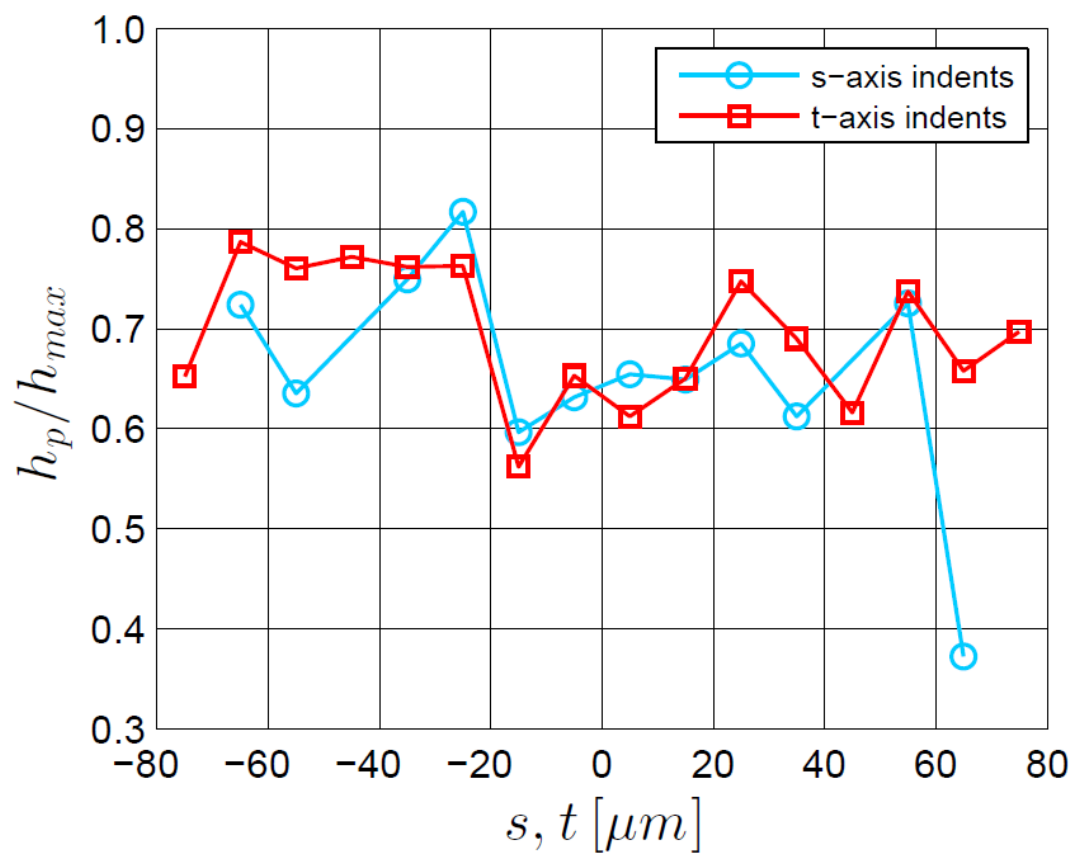


FIG.5(B)

ACCEPTED

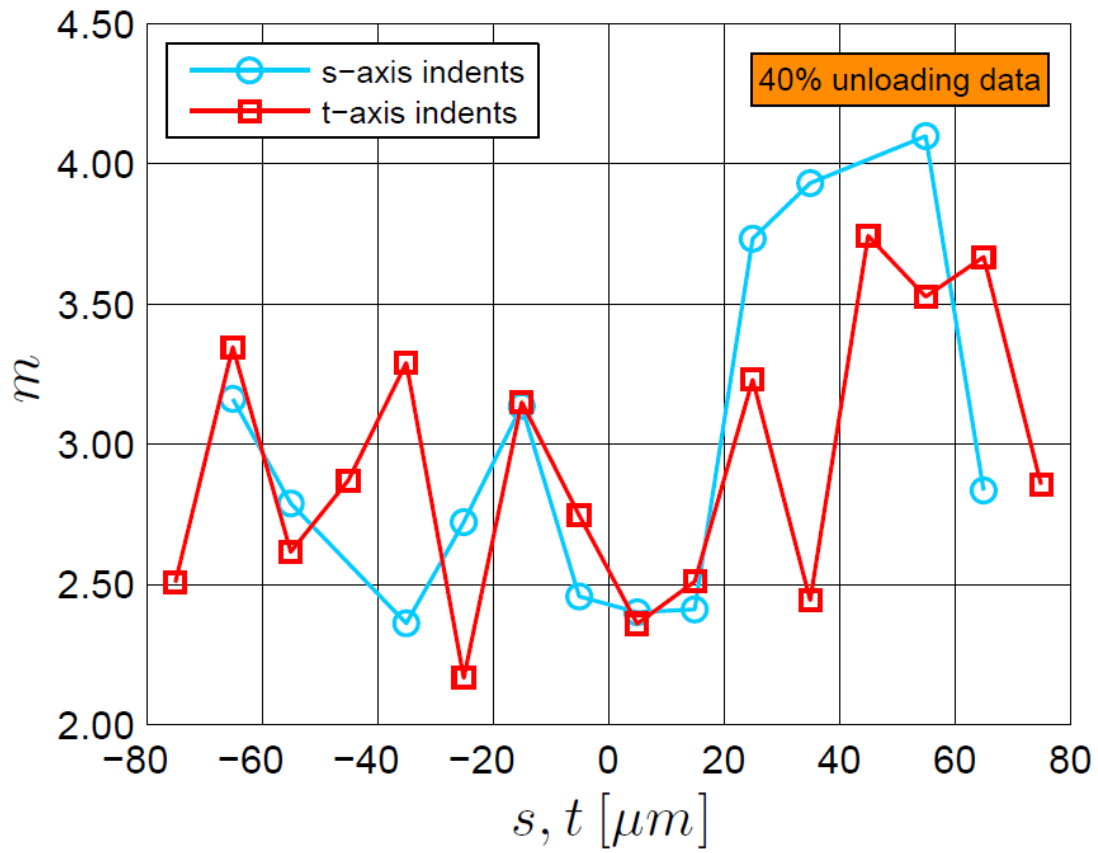


FIG.6(A)

ACCEPTED

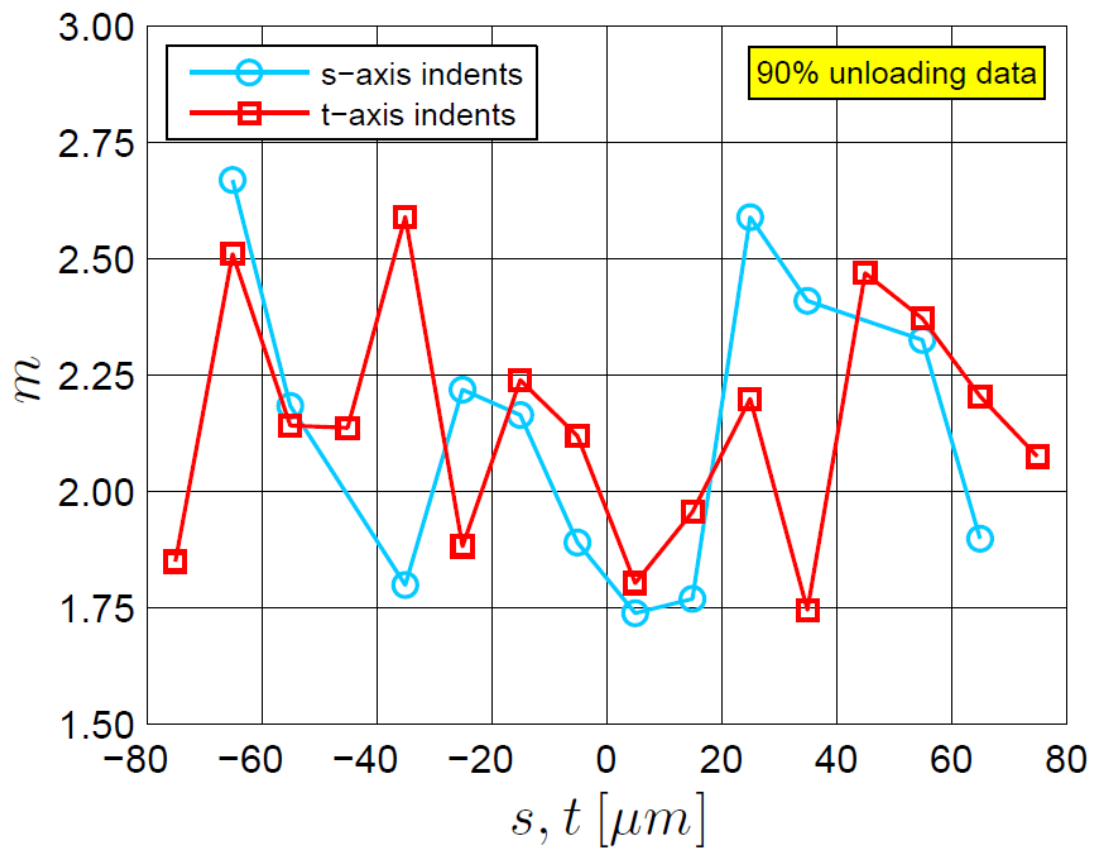


FIG.6(B)

ACCEPTED

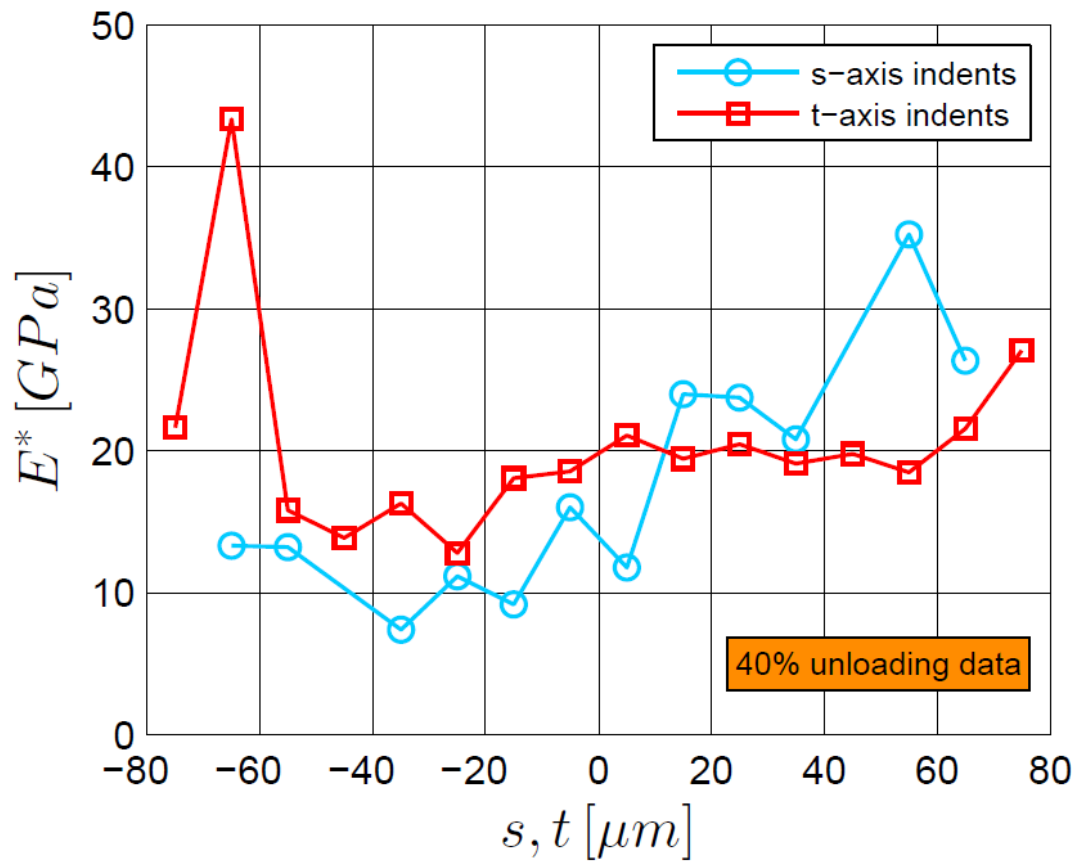


FIG.7(A)

ACCEPTED

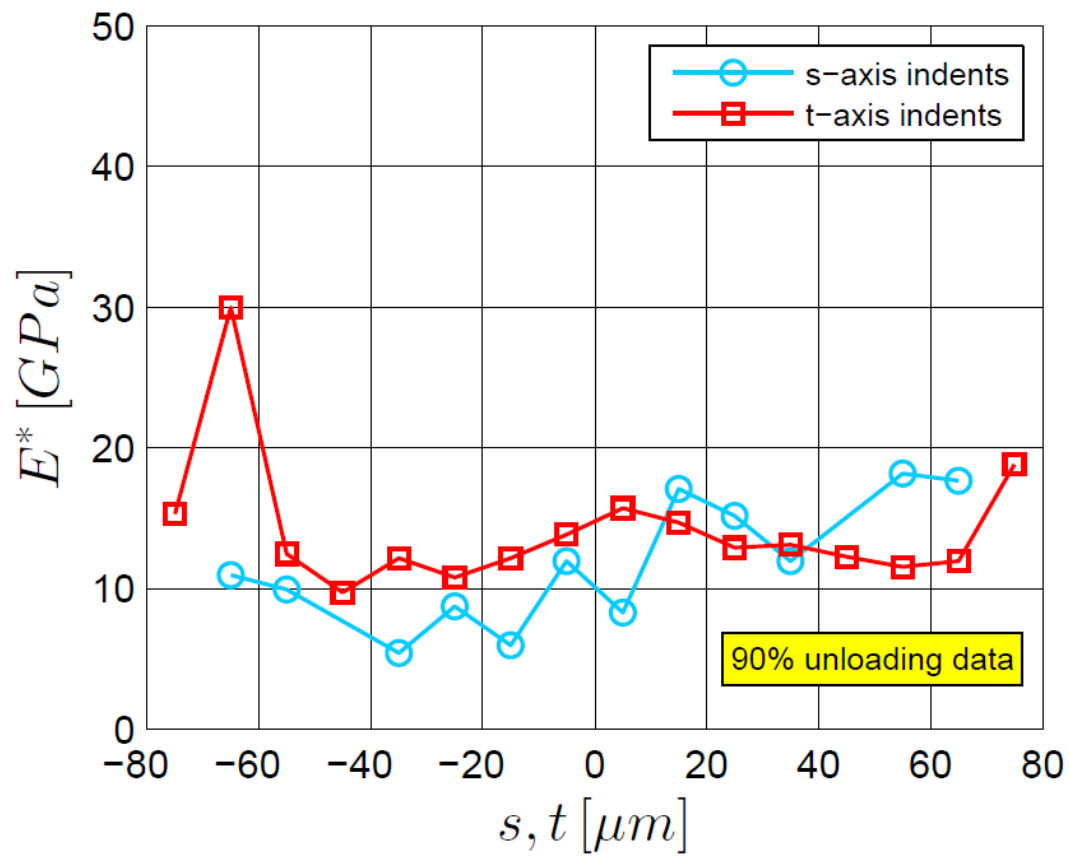


FIG.7(B)

ACCEPTED

Equatorial
section $z = 0$

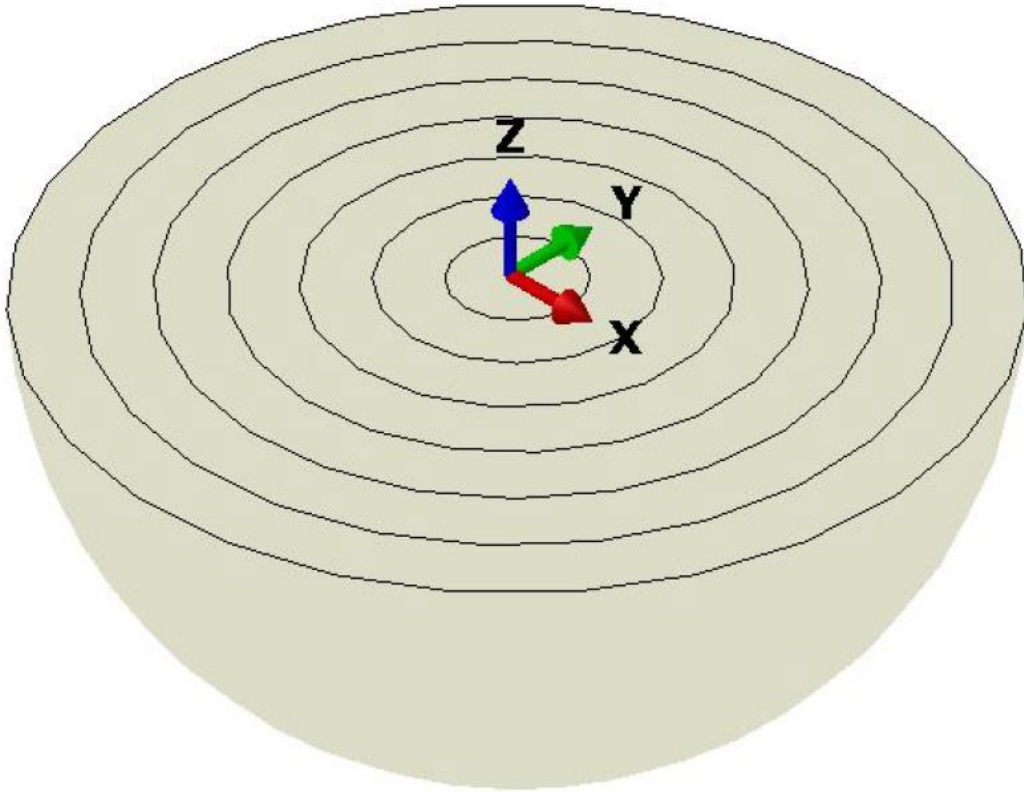


FIG.8(A)

ACCEPTED

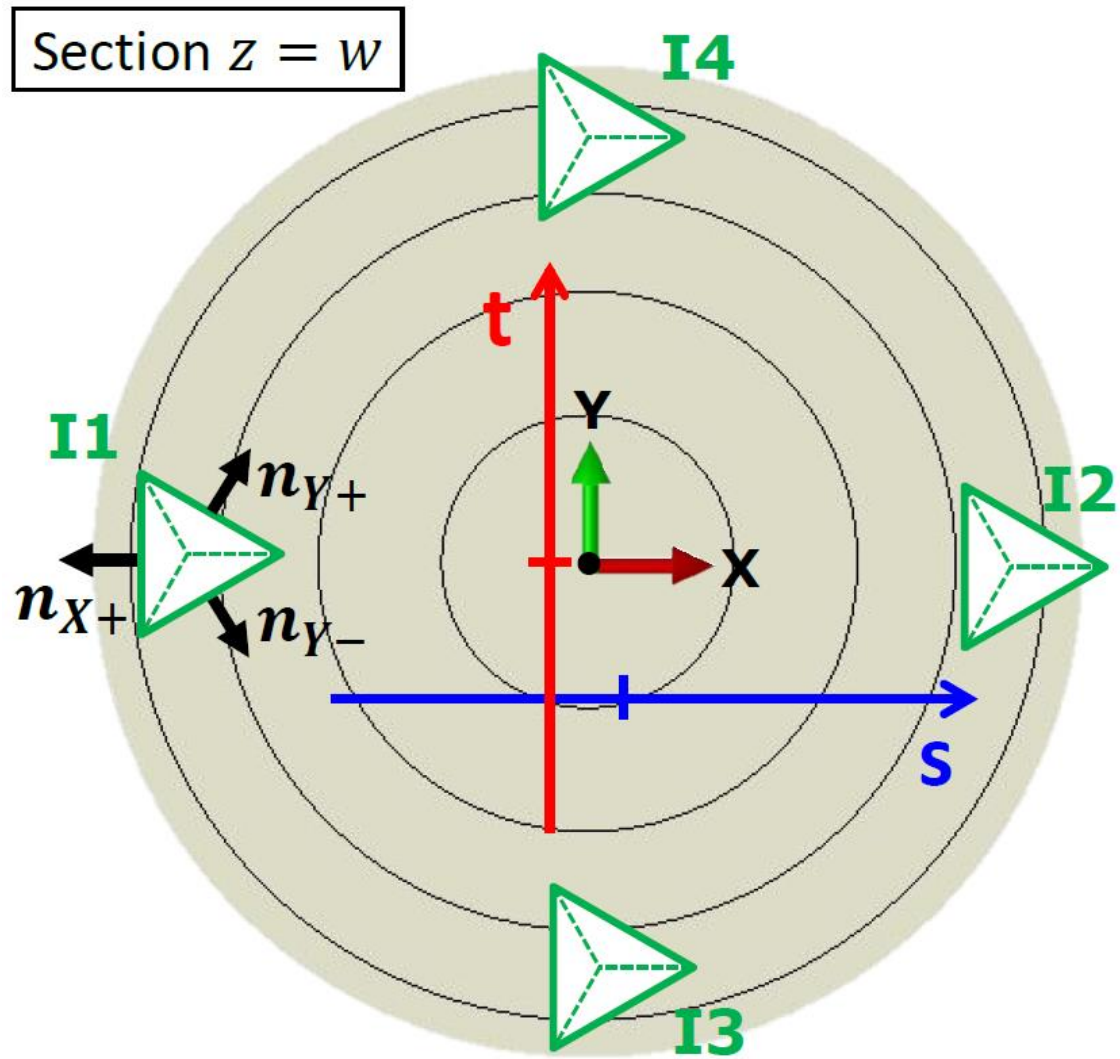


FIG.8(B)

ACCEPTED

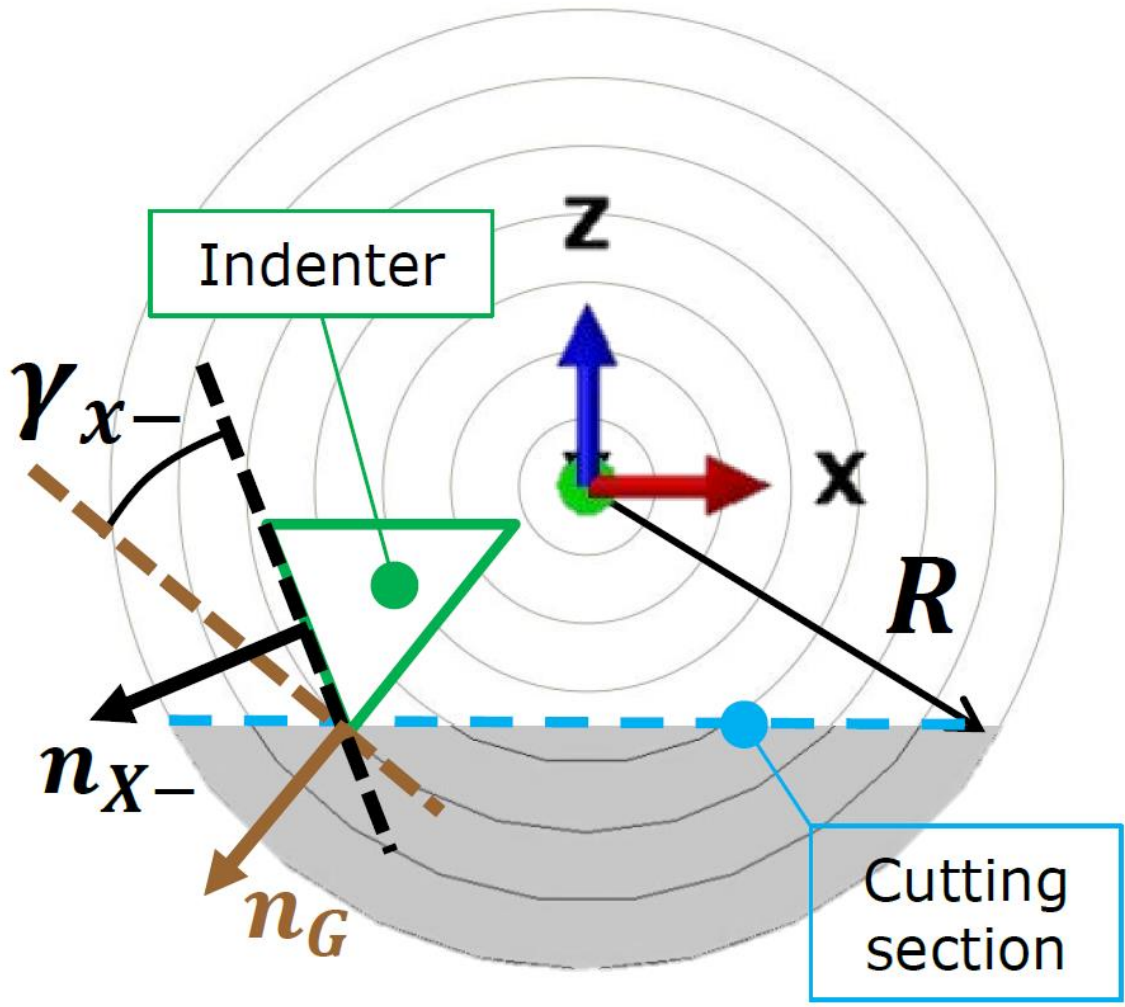


FIG.9(A)

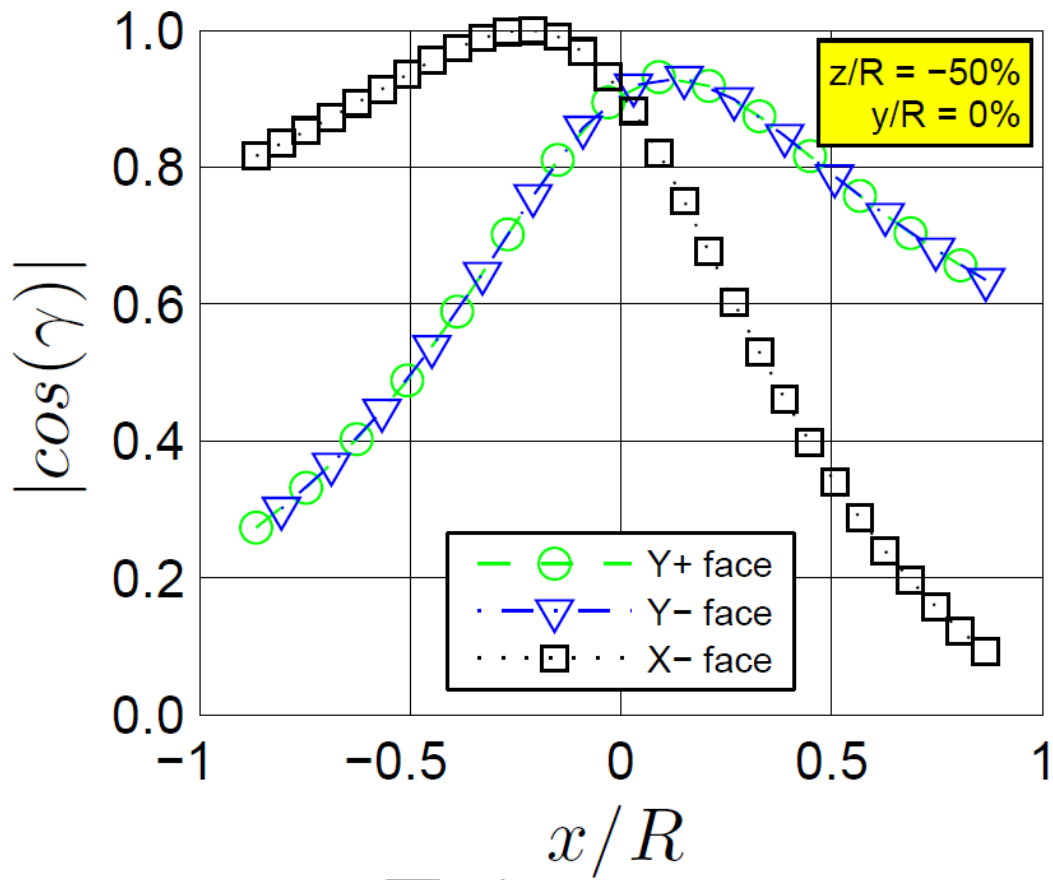


FIG.9(B)

ACCEPTED

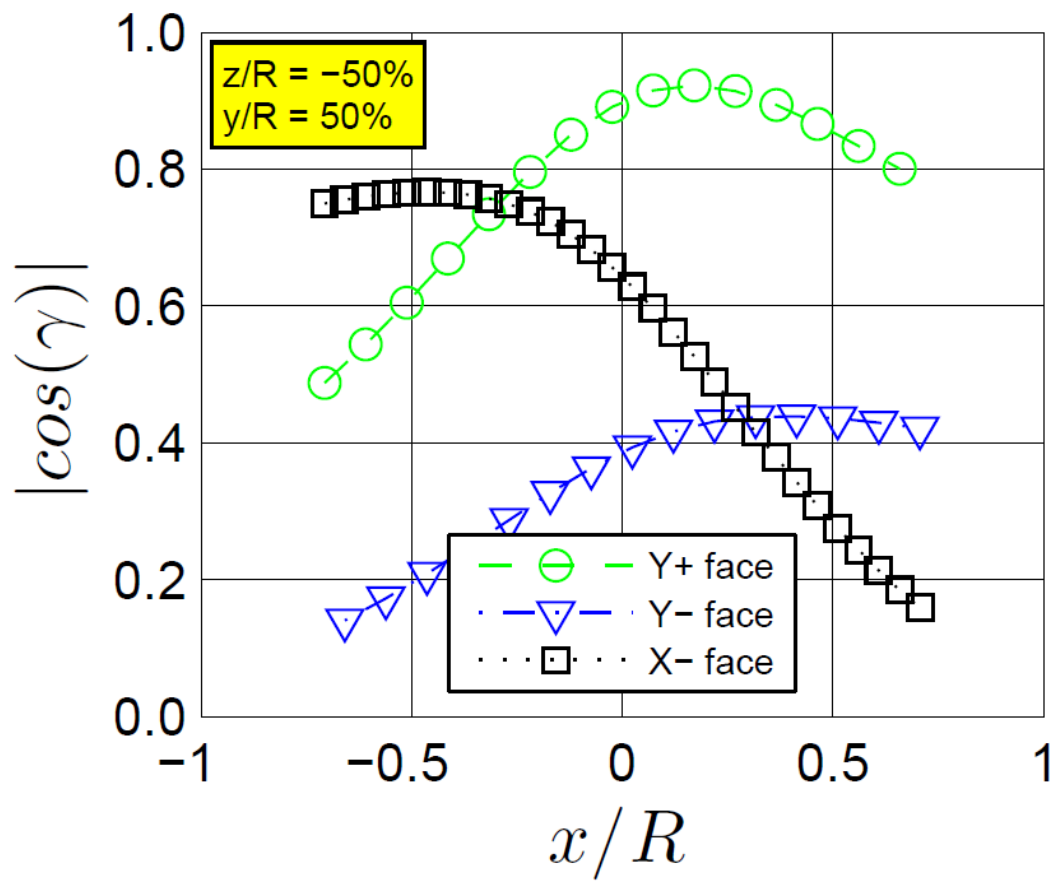


FIG.9(C)

ACCEPTED

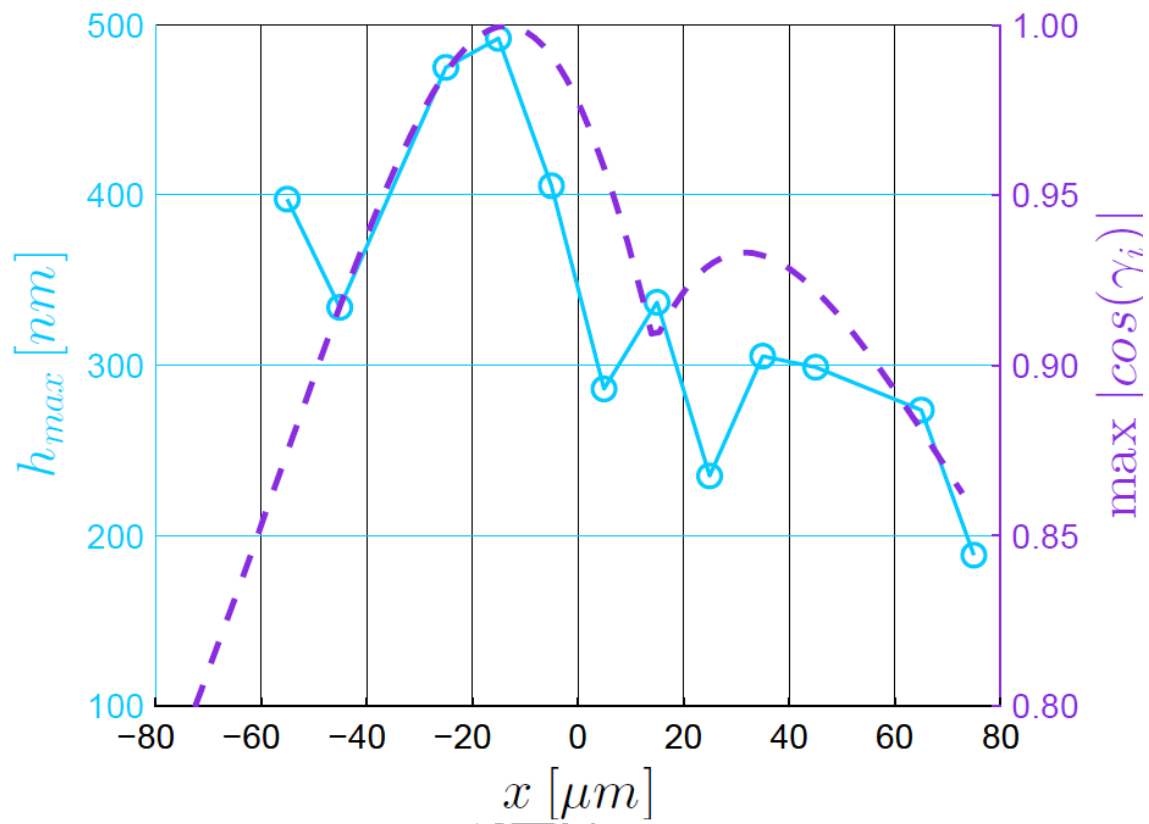


FIG.10(A)

ACCEPTED MANUSCRIPT

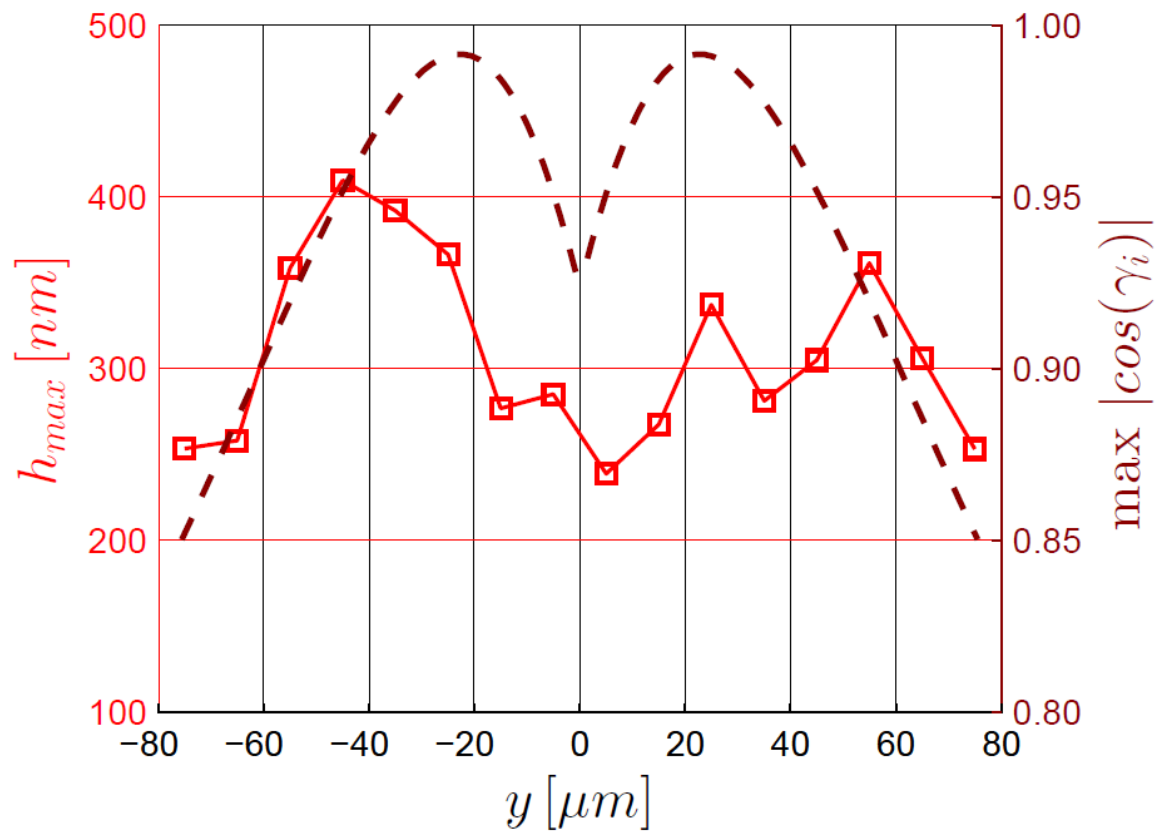


FIG.10(B)

ACCEPTED

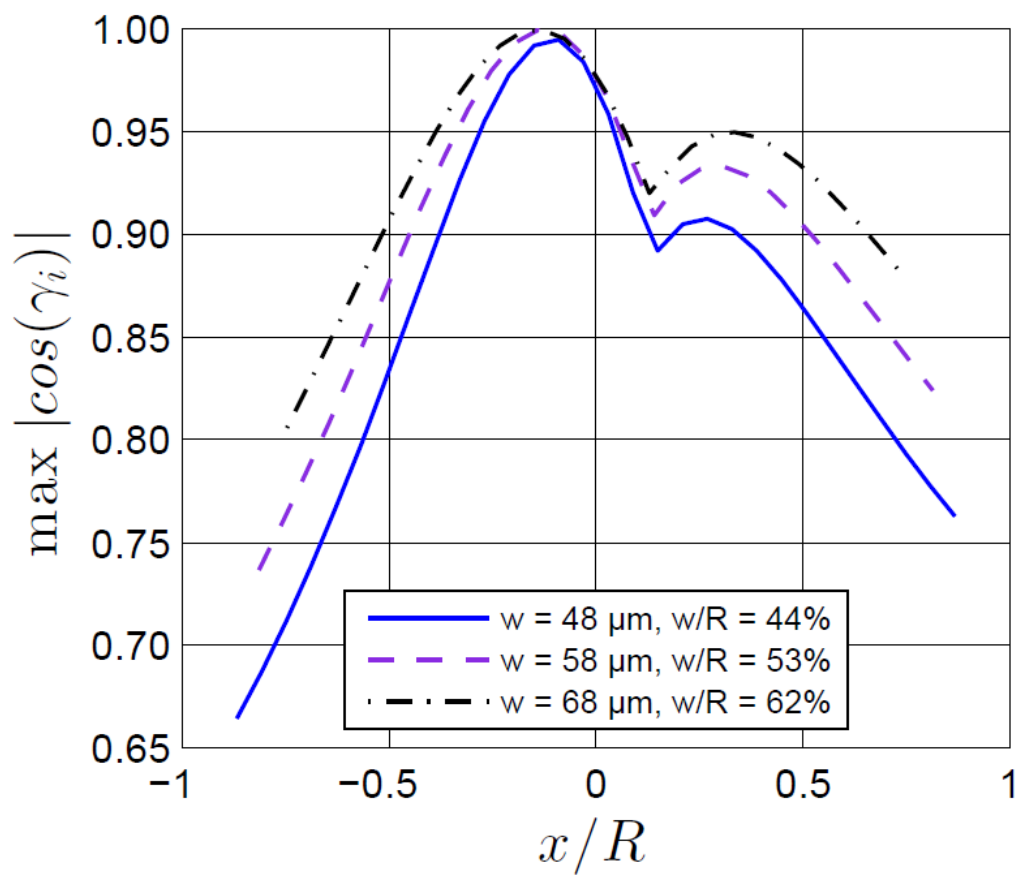


FIG.11(A)

ACCEPTED

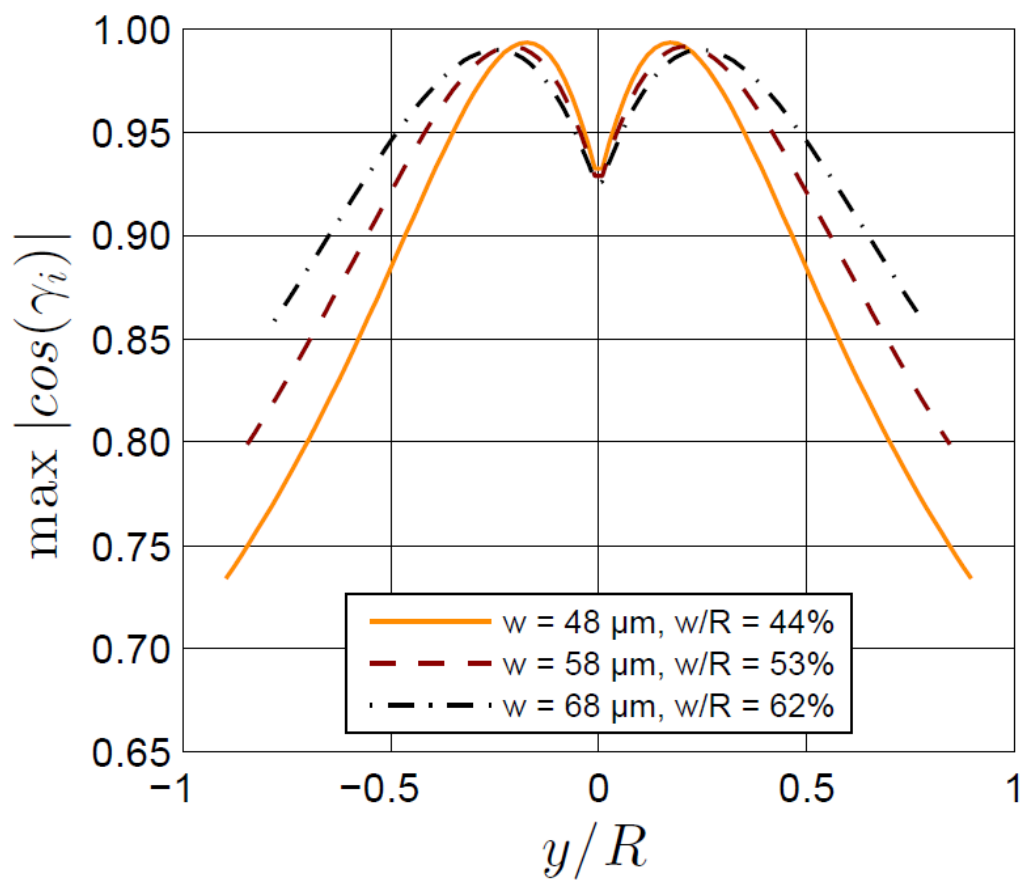


FIG.11(B)

ACCEPTED

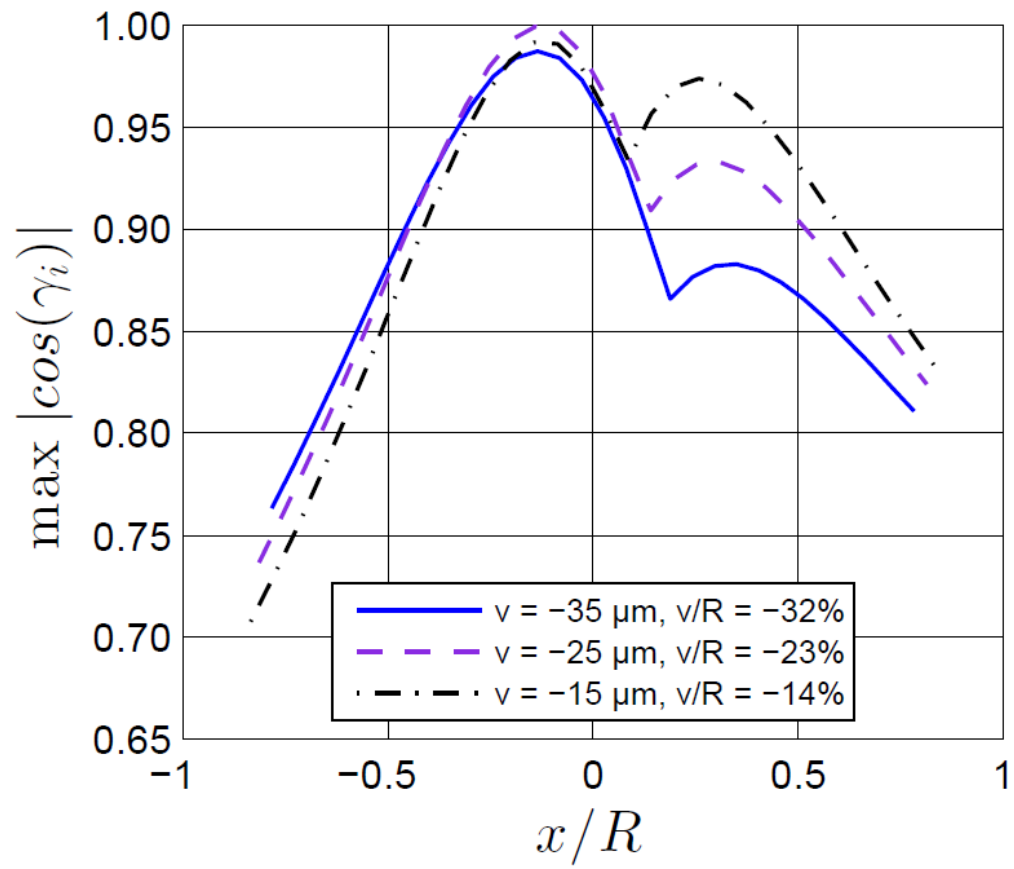


FIG.12(A)

ACCEPTED

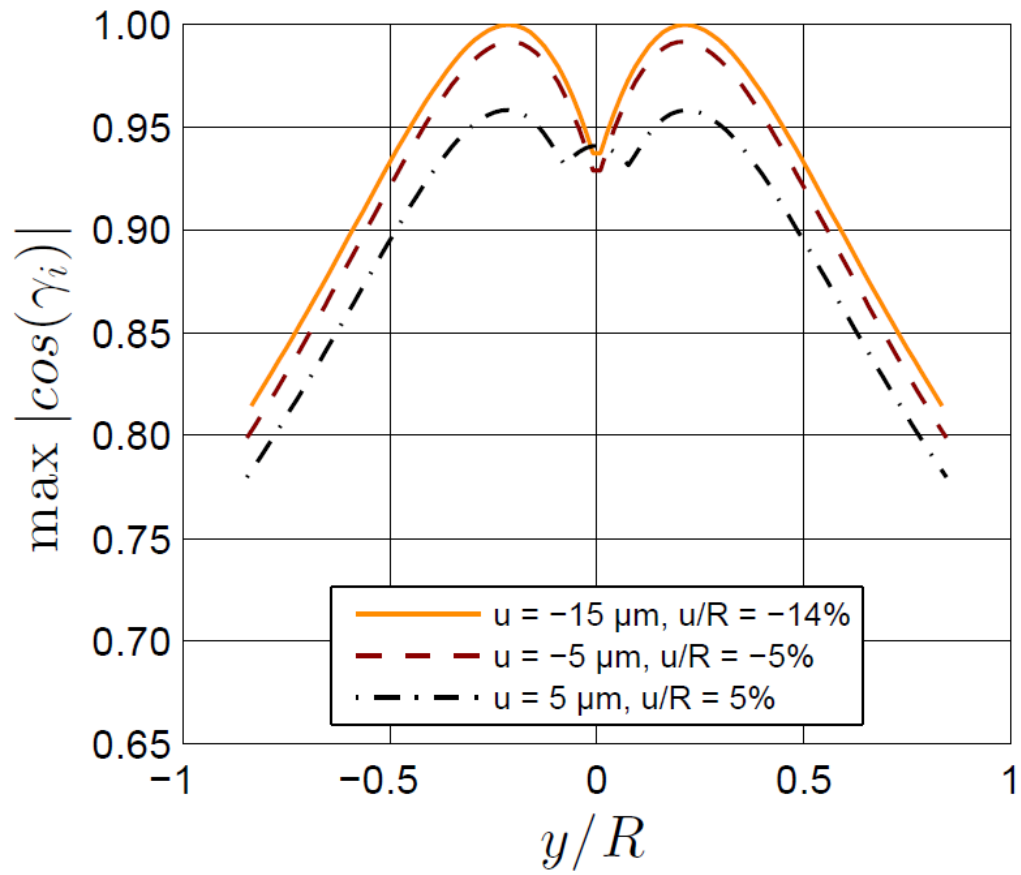


FIG12.(B)

ACCEPTED

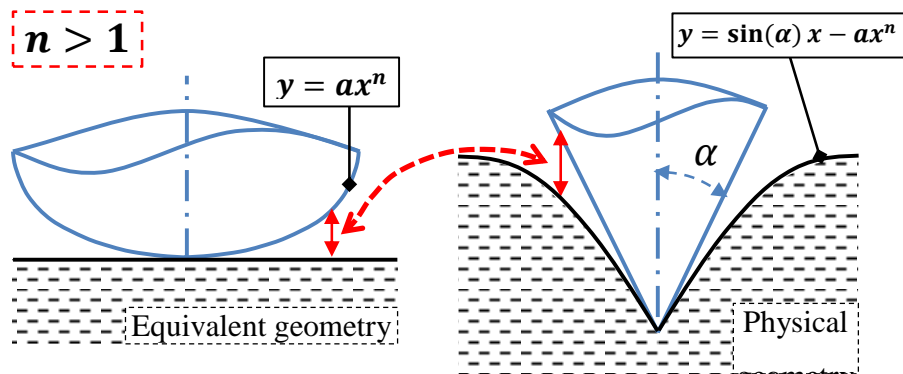


FIG.13(A)

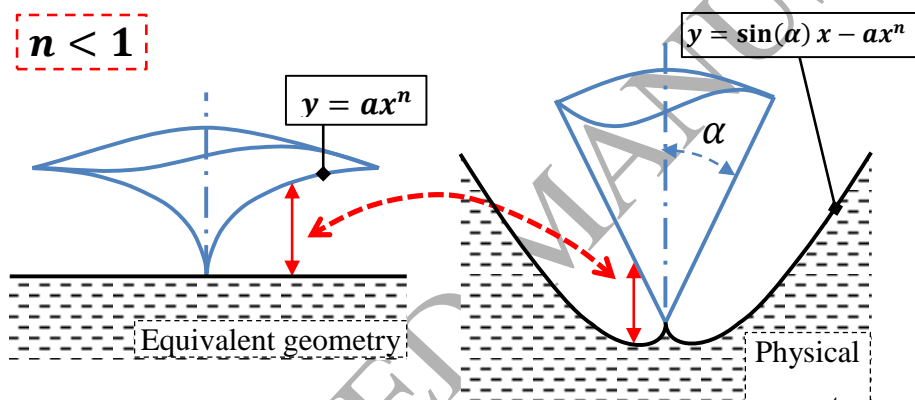
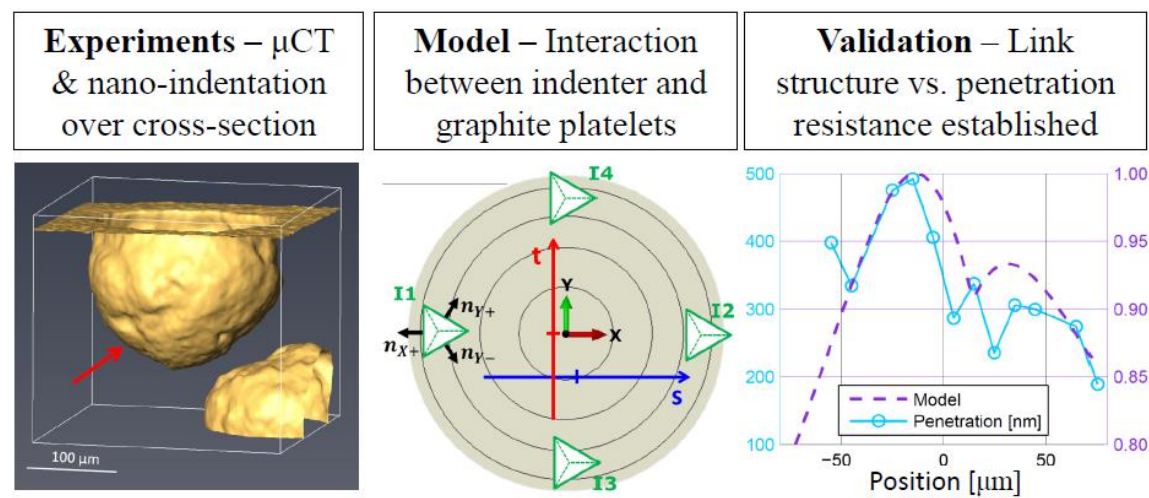


FIG.13(B)

Graphical abstract



ACCEPTED MANUSCRIPT